electrodes were sectioned to eliminate afferent signals from the heart. To insulate and fix the electrodes, the nerves and electrodes were secured with silicone glue (Kwik-Sil, World Precision Instruments, Sarasota, FL). The preamplified nerve signals were band-pass filtered at 150–1,000 Hz, full-wave rectified, and low-pass filtered at a cutoff frequency of 30 Hz by using analog circuit. After that, the neural signals were recorded at a sampling rate of 200 Hz using a 12-bit analog-to-digital converter. Pancuronium bromide (0.1 mg/kg) was administered to prevent contaminating muscular activities. At the end of the experiment, the experimental animals were killed by an overdose of intravenous pentobarbital sodium, and the background noise level of SNA was determined postmortem.

Sixteen of the 22 rabbits were used in *protocol 1 (protocols 1-1, 1-2, and 1-3)*, and the remaining 6 rabbits were used in *protocols 2, 3,* and *4*. In 10 of the 16 rabbits for *protocols 1-2* and/or *1-3* described below, we isolated both carotid sinuses from the systemic circulation by ligating the internal and external carotid arteries and other small branches originating from the carotid sinus regions. The isolated carotid sinuses were filled with warmed physiological saline through catheters inserted via the common carotid arteries. The intra-carotid sinus pressure (CSP) was controlled by a servo-controlled piston pump (model ET-126A, Labworks, Costa Mesa, CA). In the baroreflex open-loop experimental settings, bilateral vagal and aortic depressor nerves were sectioned at the neck to minimize reflex effects from cardiopulmonary regions and the aortic arch.

Electroacupuncture

Two stainless steel needles were inserted at the one-fifth point (from the knee) and the midpoint of the knee-ankle distance of approximately 30–35 mm. These needles with a diameter of 0.2 mm (CE0123, Seirin-Kasei, Shimizu City, Japan) were inserted to a depth of ~10 mm in the skin and underlying muscle (the right tibialis anterior muscle). This area corresponds to the Zusanli and Xiajuxu acupoints (over the peroneal nerve below the knee, stomach meridian, St 36 and 39) in humans.

As in previous studies (2, 3, 17, 42), the stimulus current intensity was determined as 10 times of twitch threshold, which is the minimal electrical current required for eliciting visible muscle twitches of the stimulated leg. Actually, the current was 4.8 ± 0.3 mA (4.2–5.4 mA). An electric rectangular wave current with a frequency of 1 Hz and with pulse duration of 5 ms was passed between these two needles by using an electrical stimulator (SEN-7203, Nihon Kohden) except *protocol 4* where shorter pulse durations were challenged.

Protocols

The experimental protocol was approved by the Animal Experimental Committee of National Cardiovascular Center Research Institute.

Protocol 1: effect of Zusanli electroacupuncture on AP, SNA, and baroreflex. PROTOCOL 1-1 (BAROREFLEX CLOSED-LOOP CONDITION, N = 6). To elucidate the overall cardiovascular inhibitory effects of electroacupuncture, we performed 1 Hz electroacupuncture for 8 min and measured AP and SNA responses under conditions of intact cardiovascular reflexes. In this closed-loop protocol, vagal and aortic depressor nerves were preserved. Baseline data were measured for 1 min before acupuncture insertion. At 10 min after acupuncture insertion, baseline data were measured again for 1 min. Electroacupuncture was applied for 8 min. The recovery data were measured for 2 min after the cessation of electroacupuncture.

PROTOCOL 1-2 (BAROREFLEX OPEN-LOOP CONDITION, N = 8). To elucidate the effects of electroacupuncture on the arterial baroreflex over an entire operating range, we performed a baroreflex open-loop experiment as follows: CSP was first decreased to 40 mmHg. After attainment of a steady state, CSP was increased from 40 to 160 mmHg in increments of 20 mmHg. Each pressure step was maintained for 60 s. We measured AP and SNA during the stepwise increase in CSP. Two trials (control and electroacupuncture trials) were performed on

each rabbit. The order of the trials was randomized. The electroacupuncture trial was identical to the control trial except that electroacupuncture was commenced 1 min before the initiation of stepwise increase in CSP.

PROTOCOL 1-3 (BAROREFLEX OPEN-LOOP CONDITION WITH PERONEAL DENERVATION, N = 6). To identify the afferent pathway of electroacupuncture, we examined the effects of 1 Hz electroacupuncture on the arterial baroreflex after severing the right peroneal nerve at the level of the knee joint. Estimation of the baroreflex equilibrium diagram was conducted as in *protocol 1-2* in the control and electroacupuncture trials. Four of the six rabbits had also undergone *protocol 1-2*.

Protocol 2: effects of sham (nonelectrical) acupuncture at Zusanli and control (nonspecific) electrical and nonelectrical acupunctures on AP and SNA in baroreflex closed-loop condition (n = 6). To determine whether changes in AP and SNA during Zusanli electroacupuncture are specific responses, sham and control acupunctures were conducted under the following acupuncture conditions: *1)* no acupuncture (nonacupuncture), *2)* nonelectrical acupuncture at Zusanli-Xiajuxu (St 36–39) acupoints (sham acupuncture), *3)* nonelectrical acupuncture at Guangming-Xuanzhong (gallbladder meridian, Gb 37–39) acupoints (control acupuncture), and *4)* electrical acupuncture at Guangming-Xuanzhong acupoints (control electroacupuncture). We chose Guangming-Xuanzhong as nonspecific control acupoints (*trials 3* and *4*) because these acupoints are believed to reduce leg pain without affecting the cardiovascular system, in contrast to the Zusanli-Xiajuxu acupoints. In each trial, AP and SNA were measured for a baseline duration of 1 min, under acupuncture condition (*trial 1, 2, 3,* or *4*) for 8 min, and recovery for 1 min.

Protocol 3: effect of long-term Zusanli electroacupuncture on AP and SNA in baroreflex closed-loop condition (n = 6). To clarify the effect of long-term electroacupuncture on cardiovascular system, AP and SNA were measured during and after 30 min of electroacupuncture at Zusanli-Xiajuxu acupoints. *Protocol 3* was conducted in the same manner as *protocol 1-1* except with a longer stimulation duration than *protocol 1-1* (8 min).

Protocol 4: Effect of pulse duration of Zusanli electroacupuncture on AP and SNA in baroreflex closed-loop condition (n = 6). To examine the effect of pulse duration of electroacupuncture on AP and SNA, AP and SNA were measured during electroacupuncture at Zusanli-Xiajuxu acupoints with the pulse duration increasing stepwise from 0.1 to 0.25, 0.5, 1, 2.5, 5, and 10 ms, every 60 s. In each animal, the frequency and stimulus current intensity were maintained constant as in *protocols 1, 2,* and *3*.

Data Analysis

We recorded CSP, SNA, and AP at a sampling rate of 200 Hz by using a 12-bit analog-to-digital converter. Data were stored on the hard drive of a dedicated laboratory computer system for later analyses.

In *protocol 1-1, 2, and 4*, mean AP and SNA for 1 min were calculated for baseline conditions, every minute of electroacupuncture, and recovery. In *protocol 3*, mean AP and SNA for 5 min were calculated for baseline conditions, electroacupuncture, and recovery. In *protocols 1-2* and *1-3*, we calculated mean AP and SNA during the last 10 s of each CSP step. Because the absolute magnitude of SNA depended on recording conditions, SNA was presented in arbitrary units (au). The background noise level was set at 0 au and the SNA value at the closed-loop operating point in the control trial (without electroacupuncture) was set at 100 au for each animal.

A four-parameter logistic function analysis was performed on the neural arc (CSP-SNA data pairs) and the peripheral arc (SNA-AP data pairs) as follows (11)

$$y = \frac{P_1}{1 + \exp[P_2(x - P_3)]} + P_4 \qquad (1)$$

where x and y represent the input and the output, respectively. P_1 denotes the response range (i.e., the difference between the maximum and minimum values of y), P_2 is the coefficient of gain, P_3 is the midpoint of the logistic function on the input axis, and P_4 is the minimum value of y. The maximum gain (G_{max}) is calculated from $-P_1 P_2/4$ at $x = P_3$. The parameter values were calculated by an iterative nonlinear least-squares regression known as the downhill simplex method.

Statistical Analysis

All data are presented as means ± SD. Differences were considered to be significant when $P < 0.05$. In *protocols 1-1, 2, 3,* and *4*, the effects of electroacupuncture on AP and SNA at different time intervals were evaluated by one-way ANOVA. The Dunnett's test was used for multiple comparisons. In *protocols 1-2* and *1-3*, the effects of electroacupuncture on the four parameters of the logistic functions relating to the neural and peripheral arcs, as well as on the closed-loop operating point, were examined by using a paired t-test.

RESULTS

Figure 1*A* (*protocol 1-1*) shows a typical time series of AP and SNA in response to Zusanli-Xiajuxu electroacupuncture with intact cardiovascular reflexes. AP and SNA were reduced immediately after beginning electroacupuncture, and these remained reduced during 8-min electroacupuncture. Figure 1*B* illustrates the group-averaged AP and SNA in response to electroacupuncture. AP and SNA for baseline were unchanged by acupuncture insertion alone, while these values for 8-min electroacupuncture remained decreased from baseline. These values returned to baseline level after the cessation of electroacupuncture.

Figure 2 (*protocol 1-2*) shows a typical AP and SNA response to the increments in CSP in the control (Fig. 2, *left*) and electroacupuncture (Fig. 2, *right*) trials. A stepwise increase in CSP decreased SNA and AP in both trials. In the electroacupuncture trial, the AP and SNA response ranges to CSP were attenuated compared with the control trial.

Figure 3, *A* and *B* (*protocol 1-2*), shows the averaged baroreflex neural and peripheral arcs obtained in control and electroacupuncture trials. The neural arc showed a sigmoidal relationship between CSP and SNA. In the neural arc, the response range of SNA (P_1) and midpoint of the operating
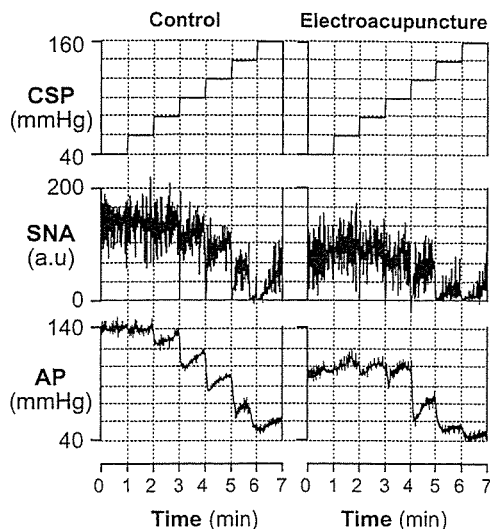

Fig. 2. Typical time series of intra-carotid sinus pressure (CSP), AP, and SNA in control (*left*) and electroacupuncture trials (*right*) in *protocol 1-2*. SNA and AP decreased in response to increments in CSP in both of the two trials. The response ranges of AP and SNA to CSP were lower in electroacupuncture than in controls.

range (P_3) were significantly decreased by electroacupuncture (Table 1). The coefficient of gain (P_2), the minimum value of SNA (P_4), and G_{max} did not differ between the two trials (Table 1). As a result, the maximum value of SNA, calculated from $P_1 + P_4$, was significantly decreased by electroacupuncture from 162 ± 31 to 130 ± 29 au ($P < 0.005$). The peripheral arc showed a more linear relationship between SNA and AP than the neural arc. In the peripheral arc, electroacupuncture did not affect any of the four parameters or G_{max} (Table 1 and Fig. 3*B*). The operating point determined by the intersection of the neural and peripheral arcs was moved toward lower AP and SNA (from *point a* to *point b*) by electroacupuncture (Fig. 3*C* and Table 1).

Figure 4 (*protocol 1-3*) shows the averaged baroreflex neural (Fig. 4*A*) and peripheral arcs (Fig. 4*B*) in control and electroacupuncture trials with severance of the peroneal nerve innervating the tibialis anterior muscle. Two arcs obtained in both trials were nearly superimposable. The four parameters and G_{max} in the neural and peripheral arcs and operating point were
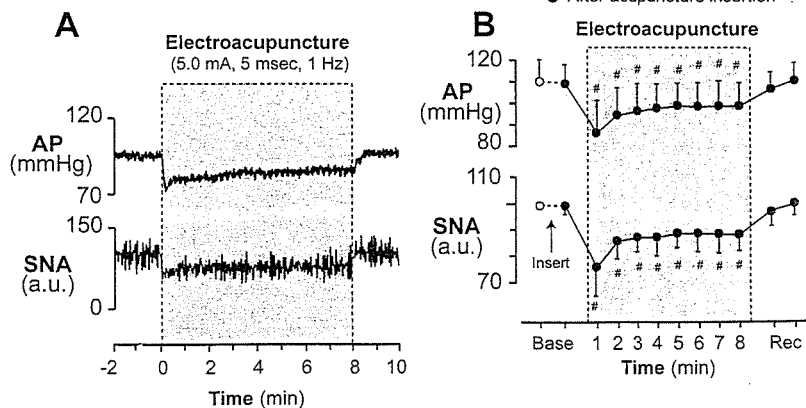

Fig. 1. Typical time series of arterial pressure (AP) and sympathetic nerve activity (SNA) during 8 min of 1-Hz electroacupuncture (*A*) and the averaged ($n = 6$) AP and SNA (*B*) in *protocol 1-1*. Data include periods of baseline (Base, 1 min), electroacupuncture (8 min), and recovery (Rec, 1 min). Each data point represents average values over 1 min. #$P < 0.05$: significantly different from baseline after acupuncture insertion. au, Arbitrary units.
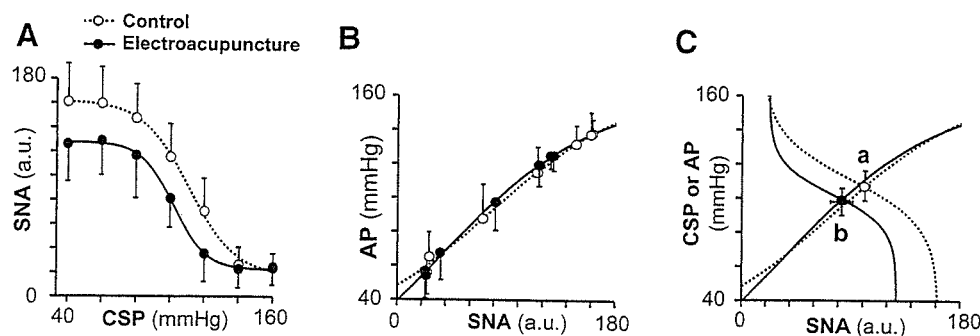
Fig. 3. Averaged ($n = 8$) baroreflex neural arc (A), peripheral arc (B), and baroreflex equilibrium diagram (C) obtained in 8 rabbits in control (O) and electroacupuncture (●) trials in *protocol 1-2*. Electroacupuncture shifted the neural arc to lower SNA (A), but it did not change the peripheral arc (B). The shift in neural arc reduced AP and SNA by 9 ± 3 mmHg and 20 ± 10 au (from *point a* to *point b*) at the operating point (C).

not affected by electroacupuncture when the peroneal nerve was denervated (Table 2 and Fig. 4C).

Figure 5 (*protocol 2*) shows the changes in AP and SNA during nonacupuncture (without acupuncture), sham acupuncture [nonelectrical acupuncture at Zusanli-Xiajuxu (St 36–39)], control acupuncture [nonelectrical acupuncture at Guangming-Xuanzhong (Gb 37–39)] and control electroacupuncture (electrical acupuncture at Gb 37–39) trials. AP and SNA did not change in these trials.

Figure 6, A and B (*protocol 3*), shows a typical time series and the averaged data, respectively, of AP and SNA in response to long-term Zusanli-Xiajuxu electroacupuncture. AP and SNA decreased immediately after electroacupuncture was started and remained reduced during 30-min electroacupuncture. In addition, AP and SNA returned to the preelectroacupuncture baseline levels immediately after cessation of electroacupuncture.

Figure 7, A and B (*protocol 4*), shows a typical time series and the averaged data, respectively, of AP and SNA during Zusanli-Xiajuxu electroacupuncture with the pulse duration increasing from 0.1 to 5 ms. Although increasing the pulse duration from 0.1 to 1 ms did not change AP and SNA, pulse durations of 2.5 ms and higher decreased SNA while pulse durations of 5 and 10 ms decreased AP.

DISCUSSION

The major new finding of the present study was that electroacupuncture at Zusanli resets the arterial baroreflex neural arc to lower SNA but does not significantly affect the baroreflex peripheral arc. As a result, the operating point determined by the intersection of the neural and peripheral arcs was moved toward lower SNA and AP by electroacupuncture. To the best of our knowledge, this is the first study delineating the effects of short-term electroacupuncture on the arterial baroreflex over an entire operating range.

Effects of Electroacupuncture on the Arterial Baroreflex (Protocol 1)

The arterial baroreflex system is one of the most important negative-feedback systems that stabilize AP against exogenous disturbances. When AP is decreased by exogenous perturbation such as blood loss, the reduction in AP is sensed by the arterial baroreceptors. SNA is then increased by the arterial baroreflex to buffer the reduction in AP. In such circumstances, SNA and AP change reciprocally. On the other hand, when SNA is changed by an exogenous perturbation such as emotional stress, SNA and AP change in parallel. In *protocol 1-1*, electroacupuncture decreased both SNA and AP, indicating that electroacupuncture introduced exogenous perturbation to decrease SNA with a resultant reduction in AP. Although the net effect of electroacupuncture is to decrease SNA, the perturbation of AP cannot be excluded. For example, because electroacupuncture also twitched the hindlimb muscles, electroacupuncture might have perturbed AP via changes in vascular resistance and/or venous return through muscle pump function. Therefore, to quantify the contribution of both perturbations on SNA and on AP, we performed *protocol 1-2*. Perturbation of AP is most easily detected by comparing AP at the same SNA level with and without electroacupuncture.

In *protocol 1-2*, we performed a baroreflex open-loop experiment and identified the static characteristics of the neural and peripheral arcs over a wide operating range. As expected, electroacupuncture shifted the neural arc toward lower SNA and decreased maximum SNA to ~80% of control (Fig. 3A). This shift is not due to reduced perfusion to the medulla by AP reduction during electroacupuncture because the AP was decreased by ~10 mmHg and would not induce cerebral ischemia. In contrast, electroacupuncture had little effect on the peripheral arc (Fig. 3B). In other words, AP with and without electroacupuncture did not differ significantly at any of the SNA levels. Therefore, changes in AP observed in *protocol 1-1*

Table 1. *Effect of electroacupuncture on the operating point of baroreflex and on the 4 parameters of logistic functions approximating neural and peripheral baroreflex arcs*

	Control	Electroacupuncture
Operating point		
Arterial pressure, mmHg	108.4±8.7	98.8±7.9†
Sympathetic nerve activity, au	99.8±4.1	80.0±8.9†
Neural arc		
P_1, au	144.0±35.0	112.6±9.2†
P_2, au/mmHg	0.08±0.03	0.09±0.09
P_3, mmHg	111.4±6.5	103.3±10.0*
P_4, au	17.5±6.1	17.4±8.7
G_{max}, au/mmHg	−2.94±0.91	−2.58±1.27
Peripheral arc		
P_1, mmHg	129.6±20.5	125.9±19.5
P_2, au/mmHg	−0.03±0.01	−0.03±0.01
P_3, au	80.6±23.2	71.7±17.1
P_4, mmHg	29.9±16.3	29.5±12.1
G_{max}, mmHg/au	0.74±0.10	0.84±0.18

Values are means ± SD ($n = 8$). G_{max}, maximum gain. See *Data Analysis* for definition of 4 parameters of logistic function. au, Arbitrary units. *$P < 0.05$ and †$P < 0.005$ vs. control.

Fig. 4. Averaged (n = 6) baroreflex neural arc (A), peripheral arc (B), and baroreflex equilibrium diagrams (C) obtained in 6 rabbits in control (O) and electroacupuncture (●) trials with peroneal denervation in *protocol 1-3*. The baroreflex neural arc, peripheral arc, and the operating point were not influenced by electroacupuncture after peroneal denervation.
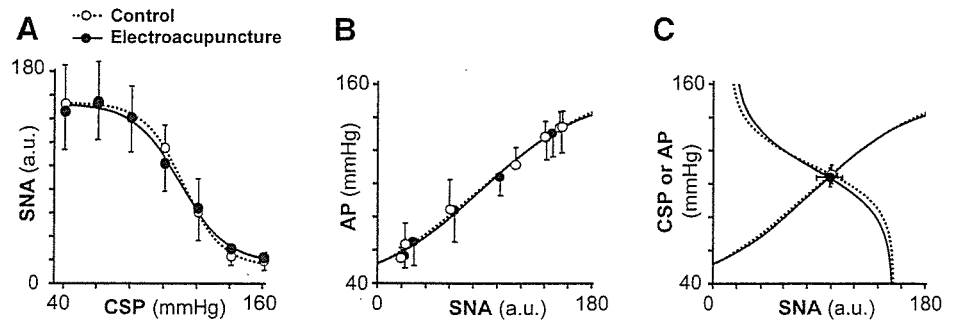
were attributable exclusively to perturbation of SNA and not to possible perturbation effects of electroacupuncture on AP.

The neural and peripheral arcs were combined to yield a baroreflex equilibrium diagram (Fig. 3C). The closed-loop operating point, determined by the intersection of the neural and peripheral arcs, moved from *point a* to *point b* during electroacupuncture. Despite a significant shift in the closed-loop operating point, neither the neural nor peripheral arc gain was altered significantly (Table 1). The fact that the baroreflex gain was maintained during electroacupuncture suggests the possible application of electroacupuncture to the treatment of cardiovascular diseases with sympathetic hyperactivity. However, the preservation of the arterial baroreflex gain in the present experimental settings may rely on normal peripheral arc characteristics. Cardiovascular diseases such as heart failure may decrease the peripheral arc gain to a variable extent due to impaired pump function. Whether the arterial baroreflex function during electroacupuncture can be maintained in cardiovascular diseases awaits future study.

Mechanisms for the Cardiovascular Inhibitory Effects of Electroacupuncture (Protocol 1)

The resetting in the baroreflex neural arc during electroacupuncture was mediated by a somatosympathetic reflex arising from the stimulated hindlimb, as evidenced by the fact that

peroneal denervation abolished the resetting (Table 2 and Fig. 4). This result was consistent with an earlier study (27) showing that depressor and sympathoinhibitory responses during acupuncture were abolished by sciatic and femoral denervation. The existence of a somatosympathetic reflex is also supported by the fact that electrical stimulation of somatic afferents reduced AP (7–9). Legramante et al. (14) showed that rapidly conducting group III somatic afferent activation can evoke AP reduction during 1-Hz electrical stimulation of the tibial nerve. In contrast, high-frequency stimulation of the somatic afferent evokes AP elevation. Passive muscle stretching, which is considered to activate group III somatic afferent fibers, shifts the baroreflex neural arc toward higher SNA, resulting in an increase in the closed-loop operating point (41). The mechanism of two opposing influences of somatic afferent activation depending on the stimulation frequency is not fully understood.

Table 2. *Effect of electroacupuncture with peroneal denervation on the operating point of baroreflex and on the 4 parameters of logistic functions approximating neural and peripheral baroreflex arcs*

	Control	Electroacupuncture
Operating point		
Arterial pressure, mmHg	105.7±5.7	104.1±5.6
Sympathetic nerve activity, au	99.8±5.1	98.3±11.1
Neural arc		
P_1, au	138.3±42.4	136.3±38.6
P_2, au/mmHg	0.11±0.03	0.08±0.03
P_3, mmHg	112.7±10.2	111.5±10.6
P_4, au	14.9±8.7	15.7±7.4
G_{max}, au/mmHg	−3.27±1.15	−2.84±1.12
Peripheral arc		
P_1, mmHg	144.1±35.5	140.5±34.4
P_2, au/mmHg	−0.02±0.002	−0.02±0.004
P_3, au	82.0±34.0	78.8±32.0
P_4, mmHg	26.1±8.1	25.5±5.3
G_{max}, mmHg/au.	0.69±0.13	0.72±0.21

Values are means ± SD (n = 6). See *Data Analysis* for definition of 4 parameters of logistic function.

-□- Non acupuncture (Rest)
-△- Sham acupuncture (St 36-39)
-○- Control acupuncture (Gb 37-39)
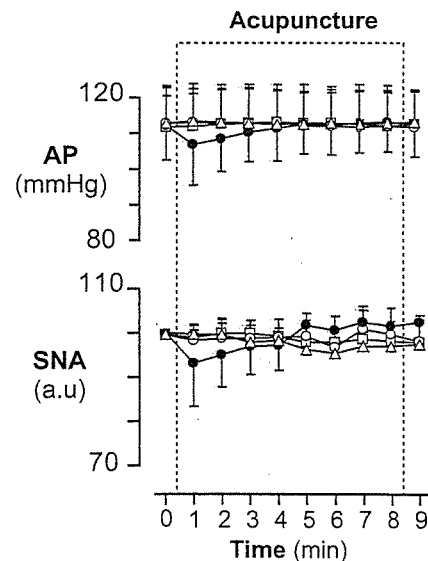-●- Control electroacupuncture (Gb 37-39)

Fig. 5. Averaged (n = 6) AP (*top*) and SNA (*bottom*) in nonacupuncture (condition without acupuncture, □), sham acupuncture [nonelectrical acupuncture at Zusanli-Xiajuxu (stomach meridian, St 36–39), △], control acupuncture [nonelectrical and acupuncture at Guangming-Xuanzhong (gallbladder meridien, Gb 37–39), ○], and control electroacupuncture [electrical acupuncture at Gb 37–39, ●] trials in *protocol 2*. Data include periods of baseline (1 min), electroacupuncture (8 min), and recovery (1 min). Each data point represents average values over 1 min.
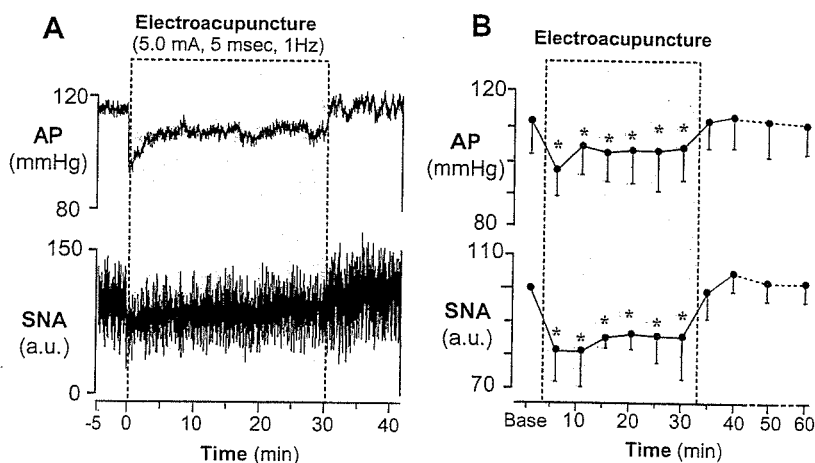
Fig. 6. Typical time series of AP and SNA during 30 min of 1-Hz electroacupuncture (St 36–39; A) and the averaged (n = 6) AP and SNA (B) in protocol 3. Data include periods of baseline (5 min), electroacupuncture (30 min), and recovery (30 min). Each data point represents averaged values over 5 min during baseline, electroacupuncture, and the first 10 min of recovery and those over 10 min during the last 20 min of recovery. *P < 0.05: significantly different from baseline after acupuncture insertion.

Another explanation for resetting in the neural arc may be circulatory endogenous opioids (e.g., β-endorphin and enkephalin), which are released from the adrenal gland and hypothalamus by prolonged (>30 min) electroacupuncture (20, 21). These endogenous opioids are known to modulate the arterial baroreflex (24, 29, 35). However, changes in endogenous opioids are unlikely to be the mechanism for reductions in SNA and AP by electroacupuncture in the present experimental settings because the inhibitory effects terminated immediately after cessation of electroacupuncture rather than lasting for several hours (42) (Fig. 1).

Previous studies suggest a central interaction between an electroacupuncture-evoked somatosympathetic reflex and the arterial baroreflex. Baroreceptor afferent inputs inhibit neural activities in the rostral ventrolateral medulla (rVLM) (6, 33). Tjen-A-Looi et al. (36) showed that electroacupuncture inhibited rVLM neural activities, suggesting that the electroacupuncture-evoked somatosympathetic reflex and arterial baroreflex share common central pathways. In addition, 2-Hz electroacupuncture inhibits SNA through the excitation of β-endorphinergic and GABAergic neurons to rVLM (12, 13).

Central interaction in the brain stem may be involved in the resetting of the arterial baroreflex neural arc induced by electroacupuncture.

Characteristics of Zusanli-Xiajuxu Electroacupuncture Used in the Present Study

The Zusanli electroacupuncture used in this study has some unique characteristics. First, our results showed that baseline AP and SNA were decreased significantly by electroacupuncture, in contrast to previous studies that found no significant reduction in baseline AP and SNA during Zusanli electroacupuncture in rats (0.5-ms duration, 1–2 mA, 2 Hz) (18) and nonelectrical acupuncture in normotensive humans (right large intestine 4, right liver 3, and left spleen 6) (22). Second, our result showed that AP and SNA were reduced as soon as electroacupuncture was started, in contrast to previous reports that the effect of Zusanli electroacupuncture did not even begin to manifest for the first 10–15 min in rats (0.5-ms duration, 1–2 mA, 2 Hz) (18) and cats (0.5-ms duration, 0.4–0.6 mA, 2–4 Hz) (37). These discrepancies may be related to the differences in acupoints and stimulation conditions (pulse duration, current, and frequency). In particular, the pulse duration used in our study (5 ms) was approximately 10–50 times longer than that used in previous studies. Indeed, the data obtained from protocol 4 show that increasing the pulse duration augments the reduction in AP and SNA during electroacupuncture; pulse durations shorter than 2.5 ms did not change AP and SNA, whereas durations of 2.5 ms and above decreased both parameters immediately after the electroacupuncture was started (Fig. 7). In addition, our data suggest that stimulation duration (<2.5 ms) does not affect arterial baroreflex, consistent with our preliminary data that baroreflex neural, peripheral, and total arcs remained unchanged during electroacupuncture with pulse durations <2.5 ms (unpublished data). These observations may indicate that the effect of electroacupuncture on arterial baroreflex is linked to the stimulation pulse duration.

The third characteristic is that the inhibitory effects of electroacupuncture on AP and SNA disappeared immediately after the cessation of electroacupuncture. In contrast, some studies showed that the inhibitory effects of electroacupuncture on AP lasted for 10–60 min after the cessation (18). The characteristics in this study may not be explained by the length of electroacupuncture because AP and SNA recovered to the
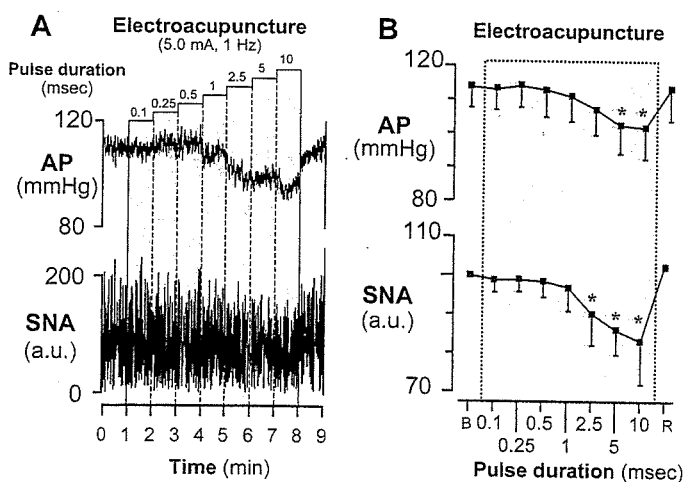

Fig. 7. Typical time series of AP and SNA during 1-Hz electroacupuncture with increasing the pulse duration (A) and the averaged (n = 6) AP and SNA (B) in protocol 4. Data include periods of baseline (B, 1 min), electroacupuncture (7 min), and recovery (R, 1 min). Each data point represents average values over 1 min. *P < 0.05; significantly different from baseline after acupuncture insertion.
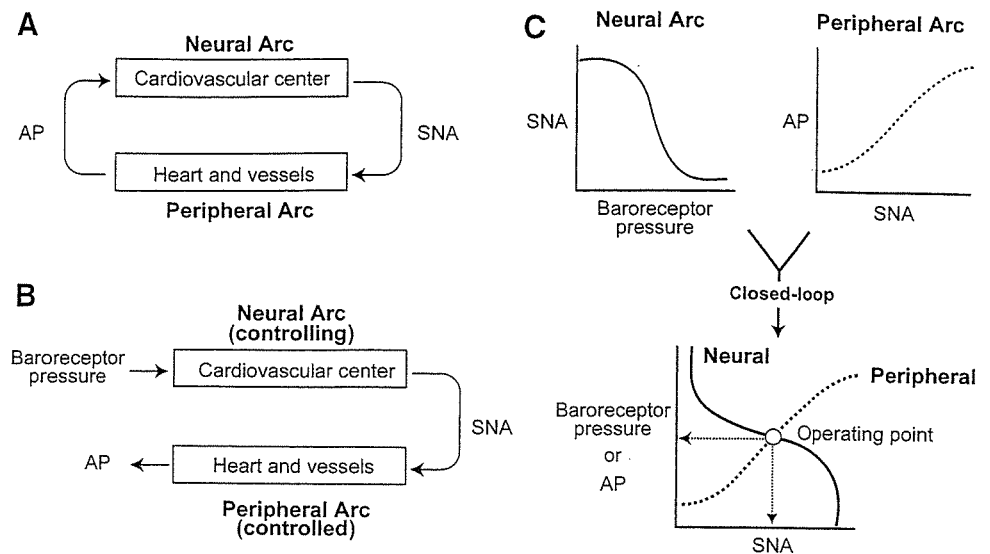
Fig. 8. Arterial baroreflex system in closed-loop (*A*) and open-loop (*B*) conditions. In open-loop conditions, the relationships between baroreceptor pressure and SNA (the neural arc) and between SNA and AP (the peripheral arc) can be quantitatively measured. Intersection of the neural and peripheral arcs corresponds to the operating point of AP and SNA under closed-loop conditions of feedback (*C*).

prestimulation baseline levels immediately after the cessation in both short-duration (8 min, Fig. 1) and longer-duration electroacupuncture (30 min, Fig. 6) protocols. The rapid disappearance of effects suggests that the AP and SNA reductions seen in the present study may not be elicited by the opioid mechanism, although clinical experiments with longer-duration electroacupuncture have demonstrated long-lasting effects on the cardiovascular system, which are attributed to opioid substances (2, 12, 15, 37, 42).

The reductions in AP and SNA during Zusanli electroacupuncture seen in the present study may not be just a nonspecific response to acupunctures. Our data from *protocol 2* (Fig. 5) showed that nonelectrical acupuncture at Zusanli (sham acupuncture) did not decrease AP and SNA, suggesting that the AP and SNA reductions during Zusanli electroacupuncture are not simply the results from insertion of acupuncture needles. Furthermore, acupuncture at Guangming-Xuanzhong (control acupuncture, control electroacupuncture) did not change AP and SNA regardless of electrical stimulation (Fig. 5). This result suggests the importance of acupoint specificity and is consistent with an earlier study showing point-specific differences in cardiovascular inhibitory responses (Jiangshi-Neiguan or Shousanli-Quchi acupoints vs. Pianli-Wenlui or Zusanli-Shangjuxu acupoints) (37). These observations may support the concept that Zusanli acupuncture changes cardiovascular variables in experimental animal models (4, 25, 28) and confers beneficial effects on cardiovascular diseases (5, 30, 34), whereas Guangming-Xuanzhong acupuncture does not affect cardiovascular variables (18).

Limitations

There are several limitations to this study. First, as anesthesia affects the autonomic nervous system, the results might have been different without anesthesia. Second, our isolation of the carotid sinus regions may stimulate carotid chemoreceptors. However, in determining baroreflex function, this factor was present in trials with and without electroacupuncture. Therefore, we believe that this factor may not affect our conclusion of baroreflex resetting during electroacupuncture.

Third, acupuncture was inserted at a point corresponding to the Zusanli acupoint in humans. When acupuncture is properly

inserted at the acupoint, the patient feels heaviness or soreness. Such sensory information is not available in an anesthetized animal. Because electroacupuncture (as distinct from acupuncture with no electrical stimulation) stimulates not only the inserted point but also the surrounding area, it has been used as a convenient way of stimulating acupoints in patients and in experimental animals. Thus, even if we failed to insert the needle at the precise acupoint, we believe that Zusanli could be stimulated electrically.

Fourth, although we determined the effects of electroacupuncture at Zusanli acupoints on cardiovascular and baroreflex systems, there are other important acupoints that are able to influence these systems. In particular, Neiguan electroacupuncture is actually known to decrease sympathetic premotor neuron activity for a longer period than Zusanli electroacupuncture (36, 37). Further studies are necessary to determine the effect of Neiguan electroacupuncture on the arterial baroreflex.

Last, we evaluated the effects of Zusanli electroacupuncture on the baroreflex function for a short acupuncture duration of only 8 min. Because electroacupuncture is typically practiced for longer periods of time, our results have limited applicability. However, the electroacupuncture we used decreased AP and SNA immediately after application, showing that the procedure has acute effect on the cardiovascular system. That was the reason why we focused on the effect of short duration electroacupuncture on the baroreflex system. Future study is necessary to examine the effects of longer-duration electroacupuncture.

In conclusion, 1 Hz, short-term electroacupuncture of Zusanli reset the baroreflex neural arc toward lower SNA but did not affect the peripheral arc. The closed-loop operating point determined by the intersection of the neural and peripheral arcs was moved toward lower SNA and AP by electroacupuncture.

APPENDIX

Theoretical Considerations: Coupling of Neural and Peripheral Arcs

Changes in AP are immediately sensed by arterial baroreceptors, which alter efferent SNA via the cardiovascular center of baroreflex (Fig. 8*A*). Efferent SNA in turn governs heart rate and the mechanical

properties of the heart and vessels, which themselves exert a direct influence over AP. This negative-feedback loop makes it difficult to analyze the behavior of the arterial baroreflex. To overcome this problem, we opened the negative-feedback loop and divided the system into controlling and controlled elements (31). We defined the controlling element as the neural arc and the controlled element as the peripheral arc (Fig. 8B). In the neural arc, the input is the pressure sensed by the arterial baroreceptors and the output is SNA. In the peripheral arc, the input is SNA and the output is AP (Fig. 8C). Because pressure sensed by the arterial baroreceptor is equilibrated with AP under physiological conditions, we superimposed the functions of the two arcs and determined the operating point of the system from the intersection of the two arcs. The operating point is defined as the AP and SNA under closed-loop conditions of the feedback system. The validity of this framework has been examined in previous studies (10, 31). Using the baroreflex equilibrium diagram, we aimed to quantify the effects of electroacupuncture on the arterial baroreflex.

GRANTS

REFERENCES

1. **Brickman AL, Calaresu FR, and Mogenson GJ.** Bradycardia during stimulation of the septum and somatic afferents in the rabbit. *Am J Physiol Regul Integr Comp Physiol* 236: R225–R230, 1979.
2. **Chao DM, Shen LL, Tjen-A-Looi S, Pitsillides KF, Li P, and Longhurst JC.** Naloxone reverses inhibitory effect of electroacupuncture on sympathetic cardiovascular reflex responses. *Am J Physiol Heart Circ Physiol* 276: H2127–H2134, 1999.
3. **Chen S and Ma SX.** Nitric oxide in the gracile nucleus mediates depressor response to acupuncture (ST36). *J Neurophysiol* 90: 780–785, 2003.
4. **Chiu DTJ and Cheng KK.** A study of the mechanism of the hypotensive effect of acupuncture in the rat. *Am J Chin Med* 2: 413–419, 1974.
5. **Chiu YJ, Chi A, and Reid IA.** Cardiovascular and endocrine effects of acupuncture in hypertensive patients. *Clin Exp Hypertens* 19: 1047–1063, 1997.
6. **Dampney RA, Horiuchi J, Tagawa T, Fontes MA, Potts PD, and Polson JW.** Medullary and supramedullary mechanisms regulating sympathetic vasomotor tone. *Acta Physiol Scand* 177: 209–218, 2003.
7. **Johansson B.** Studies on cardiovascular responses induced by electrical stimulation of afferent somatic nerves. A preliminary report. *Med Exp Int J Exp Med* 5: 447–453, 1961.
8. **Johansson B.** Circulatory responses to stimulation of somatic afferents with special reference to depressor effects from muscle nerves. *Acta Physiol Scand Suppl* 198: 1–91, 1962.
9. **Johansson B, Lundgren O, and Mellander S.** Reflex influence of "somatic pressor and depressor afferents" on resistance and capacitance vessels and on transcapillary fluid exchange. *Acta Physiol Scand* 62: 280–286, 1964.
10. **Kawada T, Shishido T, Inagaki M, Zheng C, Yanagiya Y, Uemura K, Sugimachi M, and Sunagawa K.** Estimation of baroreflex gain using a baroreflex equilibrium diagram. *Jpn J Physiol* 52: 21–29, 2002.
11. **Kent BB, Drane JW, Blumenstein B, and Manning JW.** A mathematical model to assess changes in the baroreceptor reflex. *Cardiology* 57: 295–310, 1972.
12. **Ku YH and Chang YZ.** β-Endorphin- and GABA-mediated depressor effect of specific electroacupuncture surpasses pressor response of emotional circuit. *Peptides* 22: 1465–1470, 2001.
13. **Ku YH and Zou CJ.** Beta-endorphinergic neurons in nucleus arcuatus and nucleus tractus solitarii mediated depressor-bradycardia effect of "Tinggong" 2-Hz electroacupuncture. *Acupunct Electrother Res* 18: 175–184, 1993.
14. **Legramante JM, Raimondi G, Adreani CM, Sacco S, Iellamo F, Peruzzi G, and Kaufman MP.** Group III muscle afferents evoke reflex depressor responses to repetitive muscle contractions in rabbits. *Am J Physiol Heart Circ Physiol* 278: H871–H877, 2000.
15. **Li L, Yin-Xiang C, Hong X, Peng L, and Da-Nian Z.** Nitric oxide in vPAG mediates the depressor response to acupuncture in stress-induced hypertensive rats. *Acupunct Electrother Res* 26: 165–170, 2001.
16. **Li P.** The effect of acupuncture on blood pressure: the interrelation of sympathetic activity and endogenous opeoid peptides. *Acupunct Electrother Res* 8: 45–56, 1983.
17. **Li P, Pitsillides KF, Rendig SV, Pan HL, and Longhurst JC.** Reversal of reflex-induced myocardial ischemia by median nerve stimulation: a feline model of electroacupuncture. *Circulation* 97: 1186–1194, 1998.
18. **Li P, Rowshan K, Crisostomo M, Tjen-A-Looi SC, and Longhurst JC.** Effect of electroacupuncture on pressor reflex during gastric distension. *Am J Physiol Regul Integr Comp Physiol* 283: R1335–R1345, 2002.
19. **Li P, Tjen-A-Looi S, and Longhurst JC.** Rostral ventrolateral medullary opioid receptor subtypes in the inhibitory effect of electroacupuncture on reflex autonomic response in cats. *Auton Neurosci* 89: 38–47, 2001.
20. **Lin JG, Chang SL, and Cheng JT.** Release of beta-endorphin from adrenal gland to lower plasma glucose by the electroacupuncture at Zhongwan acupoint in rats. *Neurosci Lett* 326: 17–20, 2002.
21. **Lin JG, Lo MW, Wen YR, Hsieh CL, Tsai SK, and Sun WZ.** The effect of high and low frequency electroacupuncture in pain after lower abdominal surgery. *Pain* 99: 509–514, 2002.
22. **Middlekauff HR, Yu JL, and Hui K.** Acupuncture effects on reflex responses to mental stress in humans. *Am J Physiol Regul Integr Comp Physiol* 280: R1462–R1468, 2001.
23. **Mohrman DE and Heller LJ.** *Cardiovascular Physiology* (4th ed.). New York: McGraw-Hill, 1997, p. 158–230.
24. **Moore PG, Quail AW, Cottee DB, McIlveen SA, and White SW.** Effect of fentanyl on baroreflex control of circumflex coronary conductance. *Clin Exp Pharmacol Physiol* 27: 1028–1033, 2000.
25. **Mori H, Uchida S, Ohsawa H, Noguchi E, Kimura T, and Nishijo K.** Electro-acupuncture stimulation to a hindpaw and a hind leg produces different reflex responses in sympathoadrenal medullary function in anesthetized rats. *J Auton Nerv Syst* 79: 93–98, 2000.
26. **Nishijo K, Mori H, Yosikawa K, and Yazawa K.** Decreased heart rate by acupuncture stimulation in humans via facilitation of cardiac vagal activity and suppression of cardiac sympathetic nerve. *Neurosci Lett* 227: 165–168, 1997.
27. **Ohsawa H, Okada K, Nishijo K, and Sato Y.** Neural mechanism of depressor responses of arterial pressure elicited by acupuncture-like stimulation to a hindlimb in anesthetized rats. *J Auton Nerv Syst* 51: 27–35, 1995.
28. **Ohsawa H, Yamaguchi S, Ishimaru H, Shimura M, and Sato Y.** Neural mechanism of pupillary dilation elicited by electro-acupuncture stimulation in anesthetized rats. *J Auton Nerv Syst* 64: 101–106, 1997.
29. **Petty MA and Reid JL.** The effect of opiates on arterial baroreceptor reflex function in the rabbit. *Naunyn Schmiedebergs Arch Pharmacol* 319: 206–211, 1982.
30. **Richter A, Herlitz J, and Hjalmarson A.** Effect of acupuncture in patients with angina pectoris. *Eur Heart J* 12: 175–178, 1991.
31. **Sato T, Kawada T, Inagaki M, Shishido T, Takaki H, Sugimachi M, and Sunagawa K.** New analytic framework for understanding sympathetic baroreflex control of arterial pressure. *Am J Physiol Heart Circ Physiol* 276: H2251–H2261, 1999.
32. **Si QM, Wu GC, and Cao XD.** Effects of electroacupuncture on acute cerebral infarction. *Acupunct Electrother Res* 23: 117–124, 1998.
33. **Sved AF, Ito S, and Madden CJ.** Baroreflex dependent and independent roles of the caudal ventrolateral medulla in cardiovascular regulation. *Brain Res Bull* 51: 129–133, 2000.
34. **Tam KC and Yiu HH.** The effect of acupuncture on essential hypertension. *Am J Chin Med* 3: 369–375, 1975.
35. **Taneyama C, Goto H, Kohno N, Benson KT, Sasao J, and Arakawa K.** Effects of fentanyl, diazepam, and the combination of both on arterial baroreflex and sympathetic nerve activity in intact and baro-denervated dogs. *Anesth Analg* 77: 44–48, 1993.
36. **Tjen-A-Looi SC, Li P, and Longhurst JC.** Prolonged inhibition of rostral ventral lateral medullary premotor sympathetic neurons by electroacupuncture in cats. *Auton Neurosci* 106: 119–131, 2003.

37. **Tjen-A-Looi SC, Peng L, and Longhurst JC.** Medullary substrate and differential cardiovascular responses during stimulation of specific acupoints. *Am J Physiol Regul Integr Comp Physiol* 287: R852–R862, 2004.

38. **Wang JD, Kuo TB, and Yang CC.** An alternative method to enhance vagal activities and suppress sympathetic activities in humans. *Auton Neurosci* 100: 90–95, 2002.

39. **Wong AM, Leong CP, Su TY, Yu SW, Tsai WC, and Chen CP.** Clinical trial of acupuncture for patients with spinal cord injuries. *Am J Phys Med Rehabil* 82: 21–27, 2003.

40. **Wong AM, Su TY, Tang FT, Cheng PT, and Liaw MY.** Clinical trial of electrical acupuncture on hemiplegic stroke patients. *Am J Phys Med Rehabil* 78: 117–122, 1999.

41. **Yamamoto K, Kawada T, Kamiya A, Takaki H, Miyamoto T, Sugimachi M, and Sunagawa K.** Muscle mechanoreflex induces the pressor response by resetting the arterial baroreflex neural arc. *Am J Physiol Heart Circ Physiol* 286: H1382–H1388, 2004.

42. **Yao T.** Acupuncture and somatic nerve stimulation: mechanism underlying effects on cardiovascular and renal activities. *Scand J Rehabil Med Suppl* 29: 7–18, 1993.
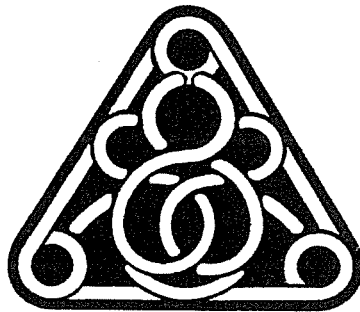
Evaluation of transmural distribution of viable muscle by myocardial strain profile and dobutamine stress echocardiography

Takeshi Maruo, Satoshi Nakatani, Yintie Jin, Kazunori Uemura, Masaru Sugimachi, Hatsue Ueda-Ishibashi, Masafumi Kitakaze, Tohru Ohe, Kenji Sunagawa and Kunio Miyatake

You might find this additional information useful...

This article cites 24 articles, 15 of which you can access free at:
http://ajpheart.physiology.org/cgi/content/full/292/2/H921#BIBL

Updated information and services including high-resolution figures, can be found at:
http://ajpheart.physiology.org/cgi/content/full/292/2/H921

Additional material and information about *AJP - Heart and Circulatory Physiology* can be found at:
http://www.the-aps.org/publications/ajpheart

This information is current as of April 5, 2007 .

Evaluation of transmural distribution of viable muscle by myocardial strain profile and dobutamine stress echocardiography

Takeshi Maruo,[1] Satoshi Nakatani,[1] Yintie Jin,[2] Kazunori Uemura,[2] Masaru Sugimachi,[2] Hatsue Ueda-Ishibashi,[3] Masafumi Kitakaze,[1] Tohru Ohe,[4] Kenji Sunagawa,[2] and Kunio Miyatake[1]

Departments of [1]Cardiology and [3]Pathology, National Cardiovascular Center, and [2]Department of Cardiovascular Dynamics, National Cardiovascular Center Research Institute, Osaka, Japan; and [4]Department of Cardiovascular Medicine, Okayama University Graduate School of Medicine, Okayama, Japan

Submitted 5 January 2006; accepted in final form 27 September 2006

Maruo T, Nakatani S, Jin Y, Uemura K, Sugimachi M, Ueda-Ishibashi H, Kitakaze M, Ohe T, Sunagawa K, Miyatake K. Evaluation of transmural distribution of viable muscle by myocardial strain profile and dobutamine stress echocardiography. *Am J Physiol Heart Circ Physiol* 292: H921–H927, 2007. First published September 29, 2006; doi:10.1152/ajpheart.00019.2006.—Transmural distribution of viable myocardium in the ischemic myocardium has not been quantified and fully elucidated. To address this issue, we evaluated transmural myocardial strain profile (TMSP) in dogs with myocardial infarction using a newly developed tissue strain imaging. TMSP was obtained from the posterior wall at the epicardial left ventricular short-axis view in 13 anesthetized open-chest dogs. After control measurements, the left circumflex coronary artery was occluded for 90 min to induce subendocardial infarction (SMI). Subsequently, latex microbeads (90 μm) were injected in the same artery to create transmural infarction (TMI). In each stage, measurements were done before and after dobutamine challenge (10 μg·kg^{-1}·min^{-1} for 10 min) to estimate transmural myocardial viability. Strain in the subendocardium in the control stage increased by dobutamine (from 53.6 ± 17.1 to 73.3 ± 21.8%, $P < 0.001$), whereas that in SMI and TMI stages was almost zero at baseline and did not increase significantly by dobutamine [from 0.8 ± 8.8 to 1.3 ± 7.0%, P = not significant (NS) for SMI, from −3.9 ± 5.6 to −1.9 ± 6.0%, P = NS for TMI]. Strain in the subepicardium by dobutamine increased in the control stage (from 23.9 ± 6.1 to 26.3 ± 6.4%, $P < 0.05$) and in the SMI stage (from 12.4 ± 7.3 to 27.1 ± 8.8%, $P < 0.005$), whereas that in the TMI stage did not change (from −1.0 ± 7.8 to −0.7 ± 8.3%, P = NS). In SMI, the subendocardial contraction was lost, but the subepicardium showed a significant increase in contraction with dobutamine. However, in TMI, even the subepicardial increase was not seen. Assessment of transmural strain profile using tissue strain imaging was a new and useful method to estimate transmural distribution of the viable myocardium in myocardial infarction.

myocardial infarction; strain; viability; echocardiography

IT IS WELL KNOWN that myocardial contraction has transmural heterogeneity. Several experimental studies confirmed that the subendocardium contributes greater to overall myocardial thickening than the subepicardium (6, 25). On the other hand, when a reduction of coronary blood flow occurs, a severe reduction of perfusion and kinesis occurs in the subendocardium, but only a trivial reduction can be detected in the subepicardium (5, 31). After a long period of ischemia, myocardial necrosis progresses from the endocardium to the epicardium (8, 13).

Myocardial strain reflects regional myocardial function. With the recent advancement of tissue Doppler echocardiography, myocardial strain can be obtained noninvasively (3, 33) and has been reported to be useful to quantify regional myocardial systolic function in ischemic heart disease (9, 11, 24, 29, 36). The recently developed myocardial strain imaging system provides us myocardial strain in each wall layer and shows its distribution in a form of transmural myocardial strain profile (TMSP; see Ref. 1). Thus combination of TMSP and dobutamine stress echocardiography (DSE), which has been used for the assessment of myocardial viability (18), is expected to demonstrate transmural distribution of viability. There have been no methods to visualize distribution of myocardial viability over the ventricular wall in myocardial infarction, and such method would provide important information in the clinical situation.

In the present study, to assess the transmural extent of myocardial infarction, we investigated TMSP in subendocardial and transmural myocardial infarction dog models and quantified the transmural heterogeneity of myocardial viability using myocardial strain imaging with DSE.

MATERIALS AND METHODS

Experimental subjects and settings. We used 13 mongrel dogs (weighing 27.3 ± 2.2 kg). After induction with intravenous pentobarbital sodium (25 mg/kg body wt), they were anesthetized with 2% isoflurane with oxygen. A median sternotomy was performed, the pericardium was split from apex to base, and, after the instrumentation, the edges of the pericardial incision were loosely resutured. A 5-Fr. micromanometer-tipped catheter (model MPC-500; Millar Instruments, Houston, TX) was positioned in the left ventricle through the apex to obtain peak systolic left ventricular pressure and peak positive and negative dP/dt. Electrocardiogram (ECG) was monitored from limb leads. Left ventricular pressure signals and ECG were digitized online. The care and use of animals was in strict accordance with the guiding principles of the American Physiological Society, and the experimental protocol was approved by the National Cardiovascular Center Committees on Animal Experiments.

Experimental protocol. A 6-Fr. sheath was placed in the right femoral artery, and an angioplasty balloon catheter was positioned in the proximal segment of the left circumflex coronary artery by the standard catheterization technique. DSE (dobutamine infusion at 10 μg·kg^{-1}·min^{-1} for 10 min) was used to assess myocardial viability. At the control stage, echocardiographic and hemodynamic measurements were done before and after DSE. A subendocardial myocardial infarction was created by inflating the balloon for 90 min

- Control

Measurement   Measurement

DSE 10 min

- SMI by coronary artery occlusion (CAO)

Inflation   Measurement

CAO 90 min   DSE 10 min   Deflation

- TMI by microbeads embolization (MBE)

Measurement

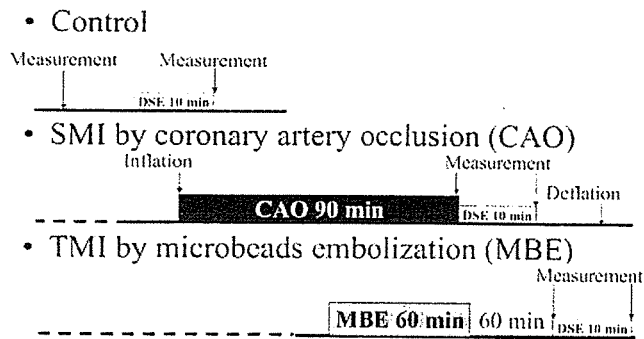MBE 60 min   60 min   DSE 10 min

Fig. 1. Experimental protocol. DSE, dobutamine stress echocardiography; SMI, subendocardial myocardial infarction; TMI, transmural myocardial infarction.

(SMI stage; see Refs. 8 and 10), and DSE was performed during balloon inflation. After balloon deflation, 200–300 mg of latex microbeads (diameter 90 μm) were slowly injected in the same artery in 60 min to create a transmural myocardial infarction (TMI stage; see Refs. 7, 12, 15). At the TMI stage, DSE was performed 60 min after microbead embolization to complete myocardial infarction and to avoid ventricular instability to dobutamine challenge, and measurements were done before and after DSE (Fig. 1).

Ultrasound data acquisition. A commercially available ultrasound scanner (PowerVision 8000 3.5-MHz transducer; Toshiba, Tokyo, Japan) was used to obtain the epicardial left ventricular short-axis images at the level of basal and midventricle by tissue Doppler imaging. Recordings were stored in the form of digital loops of two cardiac cycles with 96–102 frames/s for subsequent analysis (33).

Tissue strain imaging. Strain is defined by the equation below and expresses the deformation of an object,

$$\text{Strain} = (L - L_0)/L_0$$

where L_0 is the length of an object before deformation and L is that after or during deformation. In echocardiography, L_0 is usually a muscle length at end diastole, and myocardial strain is used to express the deformation of local myocardial segments (4, 33).

In the present study, myocardial radial strain image was obtained from off-line analysis by using a research software TDI-Q (Toshiba; see Ref. 3). To obtain a strain image, TDI-Q software first calculates the myocardial displacement of all pixels of tissue by integrating myocardial velocity over a certain period. Because the frame rate was 96–102 frames/s, the step size for integration was 9.8–10.4 ms. Next,

strain is obtained by evaluating the change of distance between pairs of two points defined on all pixels on the image by utilizing the displacement values. The distance of all two-pixel pairs at the initial time frame is equivalent to "L_0" on the above equation and set at 3 mm in this study (17). The initial time frame is set at end diastole to evaluate contraction; in other words "deformation" of the myocardium occurring in systole.

To measure local strain accurately, it is indispensable to obtain local velocity accurately. Therefore, the present myocardial strain imaging system has adopted tissue Doppler tracking and angle-correction techniques. Tissue Doppler tracking is an automatic motion tracking technique based on tissue Doppler information (30). By integrating a velocity of an indexed point on the ventricular wall known from tissue Doppler imaging, we can obtain myocardial displacement and predict the point where that point moves next. By repeating this procedure, the system can automatically track the motion of the point. With this technique, the influence of myocardial translation can be neglected. The angle-correction technique enables us to partly overcome the Doppler incident angle dependency that is inherent in Doppler echocardiography, as previous reports described (3, 26. 32). To correct the Doppler incident angle, a contraction center is set at the center of the left ventricular cavity at end systole in the left ventricular short-axis view. Next, the software automatically calculates the tissue velocity toward the contraction center (V_{motion}) by dividing the velocity toward a transducer (V_{beam}) by the cosine of the angle (θ) between the Doppler beam and the direction to the contraction center as follows:

$$V_{motion} = V_{beam}/\cos\theta$$

With the use of these two techniques, the research software TDI-Q automatically cancelled the effect of myocardial translation and angle dependency, accurately providing myocardial velocity, displacement. and strain (3). In the previously described experiments, the displacement data obtained by this method correlated with true displacement ($r = 0.99$. $P < 0.0001$; see Ref. 26).

Myocardial radial strain distribution over the myocardium is obtained as M-mode color-coded images, and the profile of distribution (TMSP) at end systole is shown as in Fig. 2. Bright color indicates high strain, and dark color indicates low strain. We obtained TMSP at basal and midinferolateral walls at end systole. We divided the myocardium into subendocardial and subepicardial half-layers by the midpoint of the myocardium at end systole. Mean strain values in the subendocardial half-layer and in the subepicardial half-layer were calculated by averaging strain values over each layer.

Fig. 2. Color-coded strain imaging, M-mode strain imaging, and transmural myocardial strain profile imaging in the control stage. *Left*: myocardial strain imaging of the left ventricular short axis at end systole. Red color means myocardial thickening. A white bar indicates an M-mode cursor. *Middle*: color-coded M-mode myocardial strain imaging obtained at the left ventricular posterior wall. The subendocardium is brighter than the subepicardium, indicating that the subendocardium contracts more vigorously. *Right*: transmural strain profile at end systole. The strain was highest at the subendocardium and lowest at the subepicardium, and the transmural strain showed a linear profile. LV, left ventricular wall.
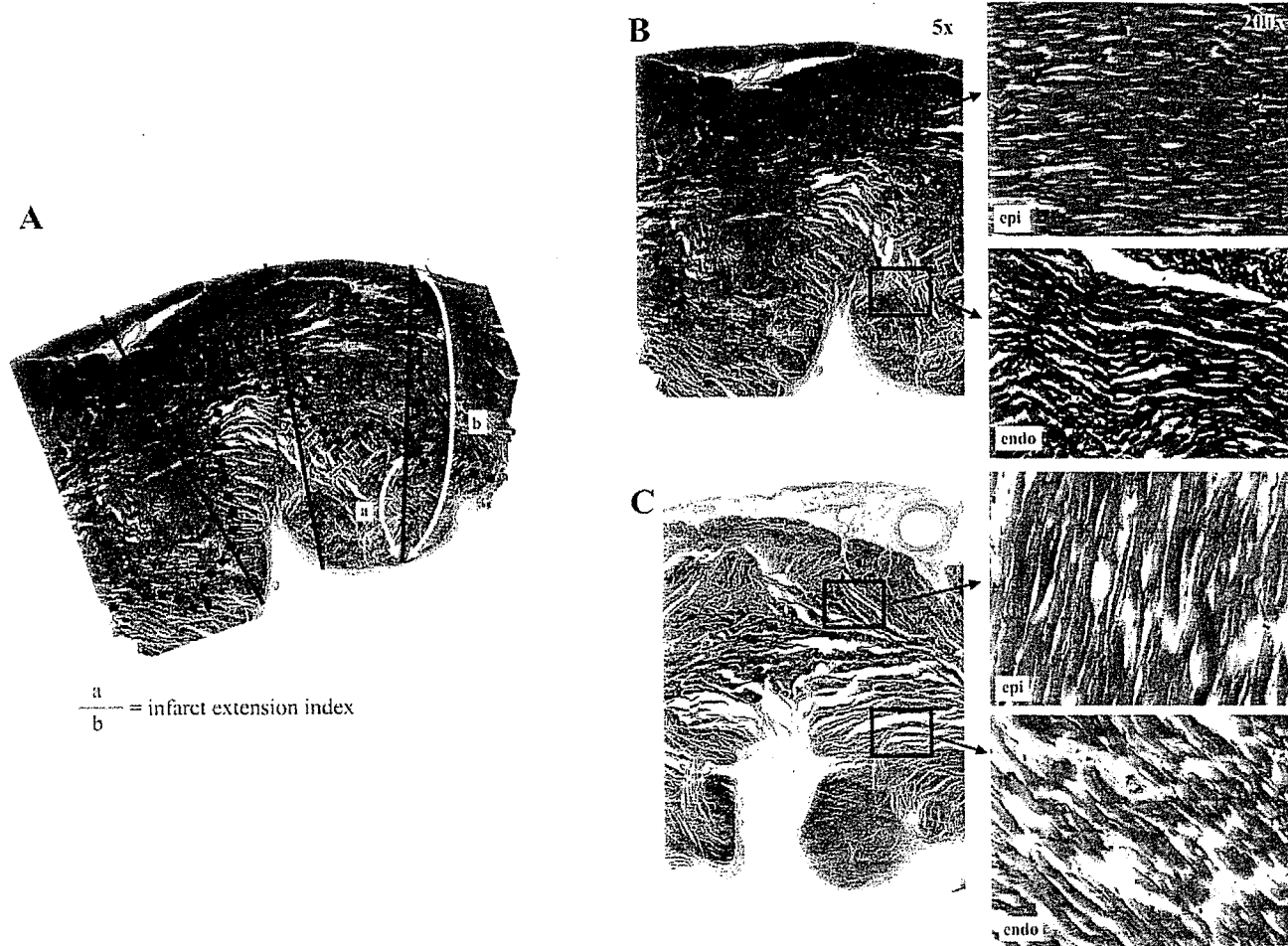
Color-coded strain image   M-mode strain image   Transmural myocardial strain profile

A

$$\frac{a}{b} = \text{infarct extension index}$$
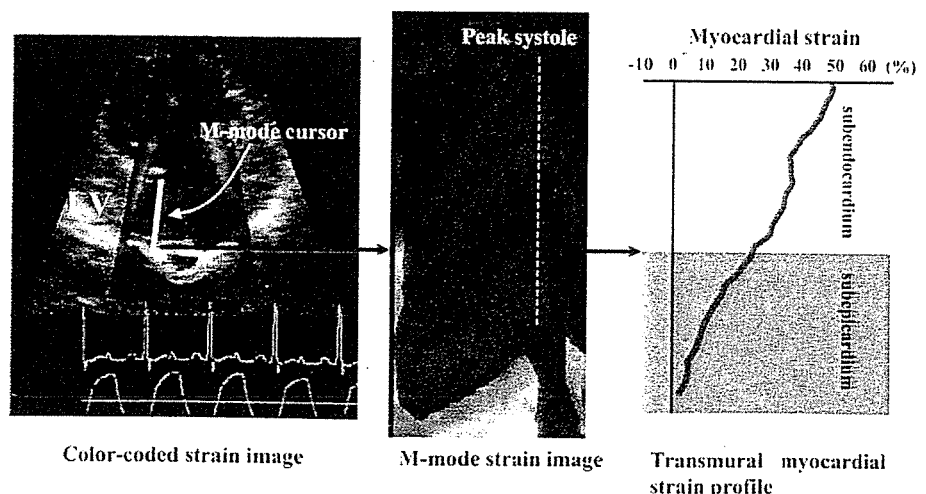
Fig. 3. *A*: determination of infarct extension index. Dotted line indicates the external limit of the infarcted zone. Examples of myocardial specimens taken after the SMI stage (*B*) and the TMI stage (*C*) stained by Masson's trichrome staining. In the SMI specimen, myocardial infarct was found only in the subendocardial layer, whereas acute ischemic changes such as wavy change or coagulation necrosis were recognized in both subendocardial and subepicardial layers in the TMI specimen. endo, Subendocardial layer; epi, subepicardial layer.

Histopathological studies. Establishment of subendocardial and transmural infarction by these techniques has been confirmed in our preliminary study and other previous studies (8, 10). We assessed the degree of extension of myocardial infarct also in the present study. At the end of the SMI stage in four dogs and the TMI stage in seven dogs, the heart was excised and cut into five to seven equally distant short-axis slices. Each slice was stained with hematoxylin-eosin and Masson's trichrome (Fig. 3). A pathologist who was blind to the experimental data examined the hearts histologically and measured

the degree of infarct extension at the basal and midinferolateral walls, as previously reported (2). On each enlarged photomicrograph of the hearts, three to five transmural radii in the infarcted area were traced perpendicular to the endocardial and epicardial borders. The distance from the endocardial border to the external limit of the infarcted zone was measured and was expressed as a percentage of the distance between the endocardial and epicardial borders as an index of infarct extension, 100% being fully transmural and 0% being no infarction.

Table 1. *Hemodynamic parameters in control, SMI, and TMI stages*

	Baseline			DSE		
	Control (*n* = 13)	SMI (*n* = 11)	TMI (*n* = 7)	Control	SMI	TMI
HR, beats/min	133±17	128±27	129±27	149±22	134±27	150±19
LVP, mmHg	123±10*†	108±24	92±21	136±11†	132±28†	112±20
+dP/d*t*, mmHg/s	2,169±484*†‡	1,577±347*†	1,207±279*	4,021±979†‡	3,231±844†	2,478±1,138
−dP/d*t*, mmHg/s	−2,531±408*†	−1,824±606*†	−1,164±465*	−3,188±650†	−2,724±892	−2,104±526

Data are presented as means ± SD; *n*, no. of dogs. DSE, dobutamine stress echocardiography; SMI, subendocardial myocardial infarction; TMI, transmural myocardial infarction; HR, heart rate; LVP, peak systolic left ventricular pressure; +dP/d*t*, peak positive dP/d*t*; −dP/d*t*, peak negative dP/d*t*. $P < 0.05$ vs. DSE values (*), vs. SMI values (‡), and vs. TMI values (†).
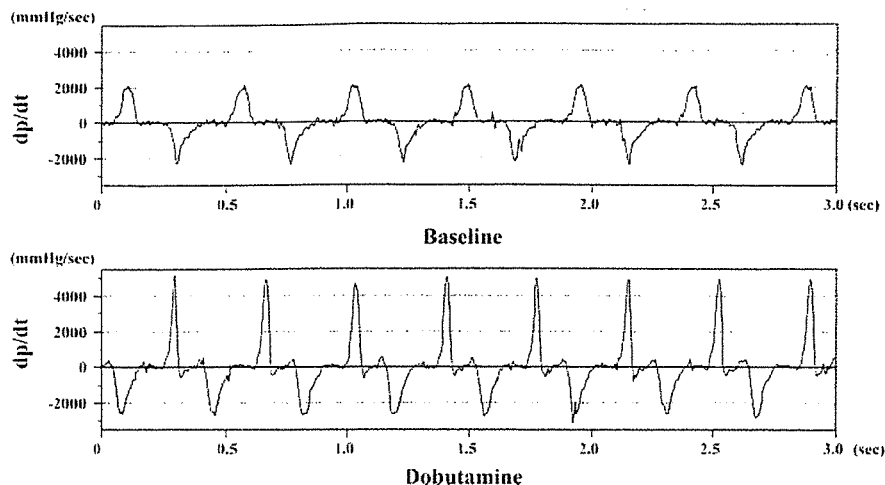
Fig. 4. dP/d*t* waveform before (*top*) and after (*bottom*) dobutamine infusion.

Reproducibility. Myocardial strain was measured by two independent observers and by one observer two times a week apart in 10 randomly selected segments to determine interobserver and intraobserver variability. The variability was assessed as the absolute difference between two measurements expressed as a percentage of their mean values. The interobserver variability was 6.5 ± 5.5 and 9.5 ± 7.5% for the subendocardial and subepicardial strains, respectively. The intraobserver variability was 7.2 ± 4.9 and 9.3 ± 3.7% for the subendocardial and subepicardial strains, respectively.

Statistical analysis. Hemodynamic data were obtained as an average of three to five consecutive beats. Statistical analyses were done with commercially available software (StatView 5.0; SAS Institute). Data are expressed as mean values ± SD. Comparisons of parameters among the stages were made by one-way ANOVA for repeated measures, followed by Scheffé's test. The Wilcoxon signed-ranks test was used to compare parameters before and after DSE. $P < 0.05$ was considered to indicate statistical significance.

RESULTS

Hemodynamic and histopathological data. Measurements were done in 13 dogs in the control stage, in 11 dogs in the SMI stage, and in 7 dogs in the TMI stage. Because of a large

infarct created by the procedure, two dogs did not survive in the SMI stage and four dogs in the TMI stage. The absolute value of peak systolic left ventricular pressure and peak positive and negative dP/d*t* decreased gradually with the advancement of the stage. However, heart rate showed no significant changes. Both positive and negative dP/d*t* significantly increased in response to dobutamine administration (Table 1 and Fig. 4).

The degree of infarct extension was assessed at 14 sites from 4 dogs after the SMI stage and at 20 sites from 7 dogs after the TMI stage. The infarct extension index was 24.9 ± 7.8% for the SMI stage and 76.1 ± 9.9% for the TMI stage. Typical examples of the histopathological findings for both subendocardial and transmural infarcts are shown in Fig. 3.

Strain value in each stage. Myocardial strain was obtained at 25 segments in the control stage, at 20 segments in the SMI stage, and 11 segments in the TMI stage. Figure 5 shows representative TMSPs in each stage. In the control stage, myocardial strain was highest in the subendocardium and declined linearly toward the subepicardium. After DSE, TMSP
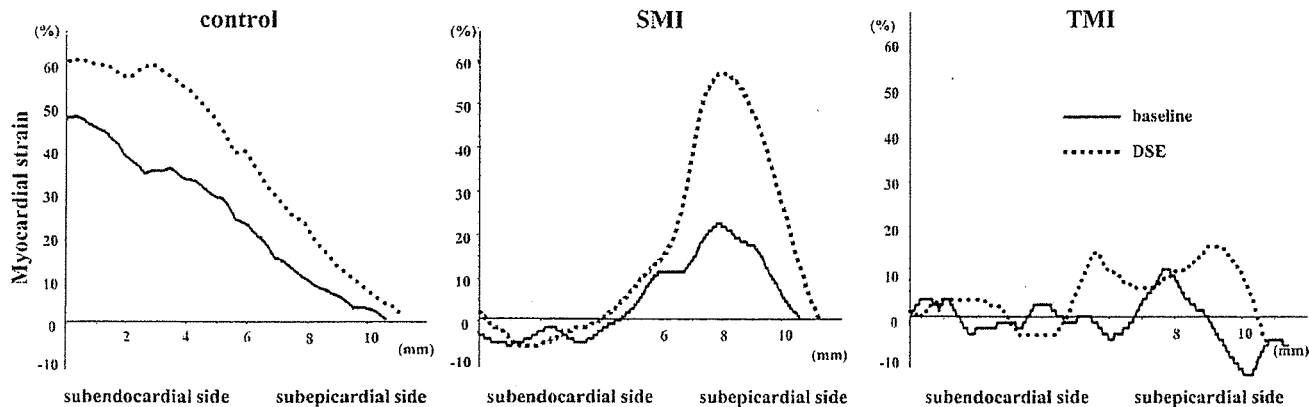

Fig. 5. Transmural myocardial strain profile before (solid lines) and after (dashed lines) dobutamine administration in each stage. *Left*: control stage. The profile was highest at the subendocardium and lowest at the subepicardium. With dobutamine administration, overall transmural myocardial strain increased. *Middle*: SMI stage. Myocardial strain at the subendocardium significantly decreased. With dobutamine administration, myocardial strain at the subepicardium showed a significant increase. *Right*: TMI stage. Overall transmural myocardial strain decreased at the baseline. Even after dobutamine administration, myocardial strain showed no significant increase.

Table 2. *Subendocardial and subepicardial strain in control, SMI, and TMI stages*

	Baseline			DSE		
	Control ($n = 25$)	SMI ($n = 20$)	TMI ($n = 11$)	Control	SMI	TMI
Endo strain	53.6±17.1*†‡	0.8±8.8	−3.9±5.6	73.3±21.8†‡	1.3±7.0	−1.9±6.0
Epi strain	23.9±6.1*†‡	12.4±7.3*†	−1.0±7.8	26.3±6.4†	27.1±8.8†	−0.7±8.3

Data are presented as means ± SD; *n*, no. of dogs. Endo strain, subendocardial strain; Epi strain, subepicardial strain. $P < 0.05$ vs. DSE values (*), vs. SMI values (‡), and vs. TMI values (†).

was uniformly uplifted, indicating the enhancement of contractility. In the SMI stage, subendocardial strain was almost zero before and after dobutamine challenge. In contrast, subepicardial strain increased after dobutamine, suggesting the presence of myocardial viability in the subepicardium. In the TMI stage, TMSP was almost flat before and after DSE, showing loss of myocardial viability through whole layers (Table 2).

Figure 6 shows changes in the subendocardial and subepicardial mean strain. Strain in the subendocardial half-layer was lower in the SMI and TMI stages than in the control stage (53.6 ± 17.1 vs. 0.8 ± 8.8 and −3.9 ± 5.6, both $P < 0.001$).
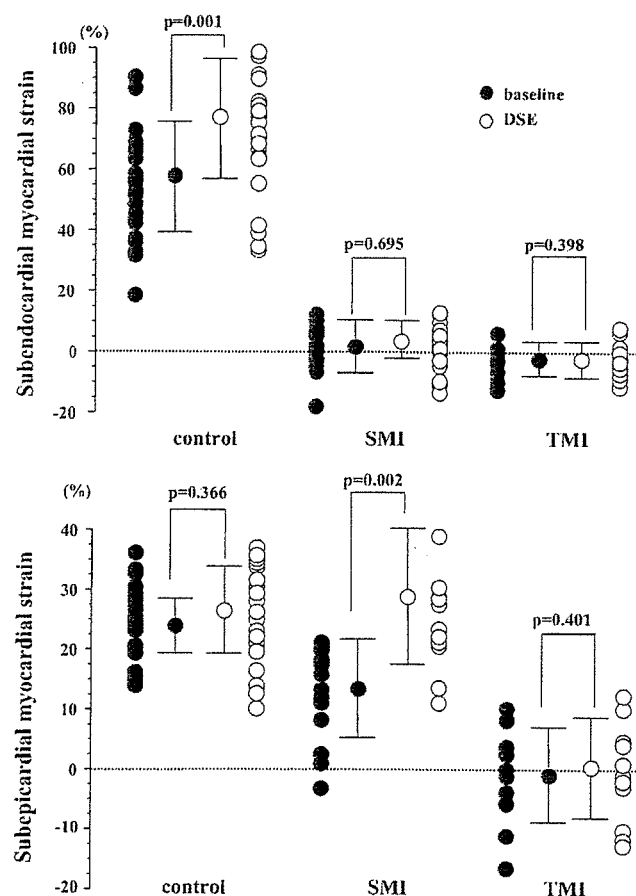

Fig. 6. Strain value in each layer. *Top*: subendocardial strain before (●) and after (○) dobutamine administration. Strain value in the subendocardial half-layer in the control stage increased with dobutamine, whereas that in the SMI and TMI stages showed no significant increase. *Bottom*: subepicardial strain before (●) and after (○) dobutamine administration. Strain value in the subepicardial half-layer in the SMI stage showed a significant increase. It showed no significant increase in the TMI stage.

There were no significant differences in the subendocardial strain between the SMI and TMI stages [P = not significant (NS)]. Strain in the subepicardial half-layer was lower in the TMI stage (−1.0 ± 7.8%) than that in the SMI stage (12.4 ± 7.3%, $P < 0.001$) and that in the control stage (23.9 ± 6.1%, $P < 0.001$).

Subendocardial strain in the control stage increased with DSE (53.6 ± 17.1 vs. 73.3 ± 21.8%, $P < 0.001$), whereas that in the SMI (0.8 ± 8.8 vs. 1.3 ± 7.0%, P = NS) and in the TMI stage (−3.9 ± 5.6 vs. −1.9 ± 6.0%, P = NS) showed no significant increase. Subepicardial strain in the control stage (23.9 ± 6.1 vs. 26.3 ± 6.4%, $P < 0.05$) and in the SMI stage (12.4 ± 7.3 vs. 27.1 ± 8.8%, $P < 0.005$) increased with DSE. It did not increase after DSE in the TMI stage (−1.0 ± 7.8 vs. −0.7 ± 8.3%, P = NS). Subepicardial strain after DSE showed no significant differences between the control and SMI stages (P = NS). These results showed that myocardial viability in the subepicardium was preserved in the SMI stage, whereas that in the TMI stage was lost.

DISCUSSION

In the present study, we analyzed the transmural distribution of viable muscle in myocardial infarction using echocardiography. Contraction in the subendocardium was lost and did not increase with dobutamine in either subendocardial infarction or transmural infarction models. On the other hand, subepicardial contraction was increased in subendocardial infarction but not in transmural infarction. These results showed that, with TMSP, we could quantify the transmural distribution of myocardial strain and identify the transmural differences in a local inotropic reserve in the viable and infarcted myocardium. The TMSP with DSE was useful to estimate the heterogeneity of transmural myocardial viability in SMI and TMI.

Transmural heterogeneity of myocardial viability. The left ventricular myocardium demonstrates transmural heterogeneity of strain distribution. It has been reported that, under normal circumstances, the subendocardial myocardium receives more blood flow and consumes more oxygen than the subepicardial one (20, 28, 35). Moreover, there is a transmural gradient of contractile function in the left ventricular wall, with greatest amount of thickening occurring in the subendocardial myocardium (6, 25). Clinically, these results were noninvasively confirmed in healthy subjects with tissue Doppler tracking technique (31). In the present study, strain value in the subendocardial layer was greater than that in the subepicardial layer in the control stage, being consistent with those of previous experimental and clinical studies. The linear decline pattern in TMSP was not observed in myocardial infarction. TMSP would potentially be useful for more detailed and innovative

evaluations of transmural myocardial function experimentally and clinically.

Effect of ischemia and dobutamine on transmural heterogeneity. After coronary artery occlusion, myocardial necrosis begins first in the endocardium and then progresses toward the epicardium with an increase in the occlusion time (8, 13). In our present study, we confirmed histologically that the SMI stage induced subendocardial infarction and the TMI stage induced transmural myocardial infarction. We observed continuous progression of myocardial dysfunction from the subendocardium to the subepicardium in myocardial infarction using echocardiography.

In acute animal models of reversible postischemic dysfunction and myocardial infarction, improved wall thickening during inotropic stimulation accurately differentiated reversible from fixed dysfunction and provided a better early assessment of viability than assessment of resting function alone (18). In clinical studies, contractile reserve by low-dose dobutamine was an independent predictor of functional recovery for myocardial infarction, which was superior to the other clinical criteria (23). In this experimental subendocardial infarction model, subendocardial strain showed no significant increase in response to inotropic stimulation, whereas subepicardial strain increased, indicating that the subepicardial myocardium was still viable. In the transmurally infarcted myocardium, myocardial strain of both subendocardium and subepicardium did not show significant increase. Therefore, the present method using TMSP and DSE is useful to visualize and quantify the contractile reserve and viability of both the subendocardium and the subepicardium.

Clinical implications. Because the prognosis of patients with subendocardial infarction is better than that with transmural infarction, assessment of the transmurality of myocardial necrosis and ischemia is an important clinical issue for patients with acute myocardial infarction or with chronic myocardial ischemia (22, 27). However, it has been difficult to make a diagnosis of subendocardial infarction by two-dimensional echocardiography. Some previous studies have shown that strain rate or strain echocardiography was useful to differentiate subendocardial infarction from transmural infarction (2, 34). We also obtained similar results using a new method of visualizing transmural myocardial strain distribution. Because the transmurality of necrosis is an important determinant of ultimate infarct size, its knowledge would be helpful in making therapeutic decisions for myocardial infarction (16, 34). Thus it is clinically helpful that we can quantify the transmural myocardial viability and necrosis extent. Furthermore, we could estimate the myocardial viability of each layer with DSE, enabling us to diagnose the stunned myocardium and predict myocardial functional recovery after myocardial infarction.

The present imaging system can be applied for the clinical evaluation of the various heart diseases characterized by subendocardial myocardial dysfunction such as anthracycline cardiotoxicity, syndrome X, hypertrophic cardiomyopathy, and dilated cardiomyopathy (14, 19, 21).

Study limitations. There was a possibility that some dogs in the subendocardial infarction models might develop transmural infarction. However, the 90-min ischemic period chosen for the subendocardial infarction models was similar to the previous studies, and it did result in subendocardial infarction (8, 10). In the present study, we showed histological evidence of suben-

docardial infarction after the SMI stage in parts of dogs. Furthermore, the difference in strain between the subendocardial and transmural infarction models was very prominent and consistent in each dog in the present study. These suggested that dogs after the SMI stage developed myocardial infarct almost only in the subendocardial layer.

We did not validate myocardial strain values using other methods, such as sonomicrometry. However, sonomicrometry is not always suitable to assess transmural distribution of myocardial strain, as shown in Fig. 5. We believe our measurement should be accurate because the displacement data obtained by our method were shown to be accurate (3, 21).

In conclusion, the quantitative analysis of transmural myocardial strain distribution could assess transmural differences in local inotropic reserve within the viable and infracted myocardium. In subendocardial infarction, the subepicardial myocardial strain showed an increase in contraction with dobutamine. However, in transmural infarction, this increase was lost. Assessment of transmural strain profile using tissue strain imaging was useful to quantify transmural distribution of the viable myocardium in SMI and TMI.

REFERENCES

1. **Chen X, Nakatani S, Hasegawa T, Maruo T, Kanzaki H, Miyatake K.** Effect of left ventricular systolic pressure on myocardial strain demonstrated by transmural myocardial strain profile. *Echocardiography* 23: 77–78, 2006.
2. **Derumeaux G, Loufoua J, Pontier G, Cribier A, Ovize M.** Tissue Doppler imaging differentiates transmural from nontransmural acute myocardial infarction after reperfusion therapy. *Circulation* 103: 589–596, 2001.
3. **Dohi K, Pinsky MR, Kanzaki H, Severyn D, Gorcsan J 3rd.** Effects of radial left ventricular dyssynchrony on cardiac performance using quantitative tissue Doppler radial strain imaging. *J Am Soc Echocardiogr* 19: 475–482, 2006.
4. **Edvardsen T, Gerber BL, Garot J, Bluemke DA, Lima JA, Smiseth OA.** Quantitative assessment of intrinsic regional myocardial deformation by Doppler strain rate echocardiography in humans: validation against three-dimensional tagged magnetic resonance imaging. *Circulation* 106: 50–56, 2002.
5. **Gallagher KP, Matsuzaki M, Koziol JA, Kemper WS, Ross J Jr.** Regional myocardial perfusion and wall thickening during ischemia in conscious dogs. *Am J Physiol Heart Circ Physiol* 247: H727–H738, 1984.
6. **Hartley CJ, Latson LA, Michael LH, Seidel CL, Lewis RM, Entman ML.** Doppler measurement of myocardial thickening with a single epicardial transducer. *Am J Physiol Heart Circ Physiol* 245: H1066–H1072, 1983.
7. **He KL, Dickstein M, Sabbah HN, Yi GH, Gu A, Maurer M, Wei CM, Wang J, Burkhoff D.** Mechanisms of heart failure with well preserved ejection fraction in dogs following limited coronary microembolization. *Cardiovasc Res* 64: 72–83, 2004.
8. **Homans DC, Pavek T, Laxson DD, Bache RJ.** Recovery of transmural and subepicardial wall thickening after subendocardial infarction. *J Am Coll Cardiol* 24: 1109–1116, 1994.
9. **Jamal F, Strotmann J, Weidemann F, Kukulski T, D'hooge J, Bijnens B, Van de Werf F, De Scheerder I, Sutherland GR.** Noninvasive quantification of the contractile reserve of stunned myocardium by ultrasonic strain rate and strain. *Circulation* 104: 1059–1065, 2001.
10. **Kim WG, Shin YC, Hwang SW, Lee C, Na CY.** Comparison of myocardial infarction with sequential ligation of the left anterior descend-

ing artery and its diagonal branch in dogs and sheep. *Int J Artif Organs* 26: 351–357, 2003.

11. **Kukulski T, Jamal F, Herbots L, D'hooge J, Bijnens B, Hatle L, De Scheerder I, Sutherland GR.** Identification of acutely ischemic myocardium using ultrasonic strain measurements. A clinical study in patients undergoing coronary angioplasty. *J Am Coll Cardiol* 41: 810–819, 2003.

12. **Lavine SJ, Prcevski P, Held AC, Johnson V.** Experimental model of chronic global left ventricular dysfunction secondary to left coronary microembolization. *J Am Coll Cardiol* 18: 1794–1803, 1991.

13. **Lowe JE, Cummings RG, Adams DH, Hull-Ryde EA.** Evidence that ischemic cell death begins in the subendocardium independent of variations in collateral flow or wall tension. *Circulation* 68: 190–202, 1983.

14. **Maier SE, Fischer SE, McKinnon GC, Hess OM, Krayenbuehl HP, Boesiger P.** Evaluation of left ventricular segmental wall motion in hypertrophic cardiomyopathy with myocardial tagging. *Circulation* 86: 1919–1928, 1992.

15. **Malyar NM, Lerman LO, Gossl M, Beighley PE, Ritman EL.** Relation of nonperfused myocardial volume and surface area to left ventricular performance in coronary microembolization. *Circulation* 110: 1946–1952, 2004.

16. **Mann DL, Gillam LD, Mich R, Foale R, Newell JB, Weyman AE.** Functional relation between infarct thickness and regional systolic function in the acutely and subacutely infarcted canine left ventricle. *J Am Coll Cardiol* 14: 481–488, 1989.

17. **Matre K, Fannelop T, Dahle GO, Heimdal A, Grong K.** Radial strain gradient across the normal myocardial wall in open-chest pigs measured with Doppler strain rate imaging. *J Am Soc Echocardiogr* 18: 1066–1073, 2005.

18. **Mercier JC, Lando U, Kanmatsuse K, Ninomiya K, Meerbaum S, Fishbein MC, Swan HJ, Ganz W.** Divergent effects of inotropic stimulation on the ischemic and severely depressed reperfused myocardium. *Circulation* 66: 397–400, 1982.

19. **Mortensen SA, Olsen HS, Baandrup U.** Chronic anthracycline cardiotoxicity: haemodynamic and histopathological manifestations suggesting a restrictive endomyocardial disease. *Br Heart J* 55: 274–282, 1986.

20. **Oh BH, Volpini M, Kambayashi M, Murata K, Rockman HA, Kassab GS, Ross J Jr.** Myocardial function and transmural blood flow during coronary venous retroperfusion in pigs. *Circulation* 86: 1265–1279, 1992.

21. **Panting JR, Gatehouse PD, Yang GZ, Grothues F, Firmin DN, Collins P, Pennell DJ.** Abnormal subendocardial perfusion in cardiac syndrome X detected by cardiovascular magnetic resonance imaging. *N Engl J Med* 346: 1948–1953, 2002.

22. **Picano E, Sicari R, Landi P, Cortigiani L, Bigi R, Coletta C, Galati A, Heyman J, Mattioli R, Previtali M, Mathias W Jr, Dodi C, Minardi G, Lowenstein J, Seveso G, Pingitore A, Salustri A, Raciti M.** Prognostic value of myocardial viability in medically treated patients with global left ventricular dysfunction early after an acute uncomplicated myocardial infarction: a dobutamine stress echocardiographic study. *Circulation* 98: 1078–1084, 1998.

23. **Pierard LA, De Landsheere CM, Berthe C, Rigo P, Kulbertus HE.** Identification of viable myocardium by echocardiography during dobutamine infusion in patients with myocardial infarction after thrombolytic therapy: comparison with positron emission tomography. *J Am Coll Cardiol* 15: 1021–1031, 1990.

24. **Pislaru C, Bruce CJ, Anagnostopoulos PC, Allen JL, Seward JB, Pellikka PA, Ritman EL, Greenleaf JF.** Ultrasound strain imaging of altered myocardial stiffness: stunned versus infarcted reperfused myocardium. *Circulation* 109: 2905–2910, 2004.

25. **Sabbah HN, Marzilli M, Stein PD.** The relative role of subendocardium and subepicardium in left ventricular mechanics. *Am J Physiol Heart Circ Physiol* 240: H920–H926, 1981.

26. **Sade LE, Severyn DA, Kanzaki H, Dohi K, Gorcsan J 3rd.** Second-generation tissue Doppler with angle-corrected color-coded wall displacement for quantitative assessment of regional left ventricular function. *Am J Cardiol* 92: 554–560, 2003.

27. **Sawada S, Bapat A, Vaz D, Weksler J, Fineberg N, Greene A, Gradus-Pizlo I, Feigenbaum H.** Incremental value of myocardial viability for prediction of long-term prognosis in surgically revascularized patients with left ventricular dysfunction. *J Am Coll Cardiol* 42: 2099–2105, 2003.

28. **Sjoquist PO, Duker G, Almgren O.** Distribution of the collateral blood flow at the lateral border of the ischemic myocardium after acute coronary occlusion in the pig and the dog. *Basic Res Cardiol* 79: 164–175, 1984.

29. **Skulstad H, Urheim S, Edvardsen T, Andersen K, Lyseggen E, Vartdal T, Ihlen H, Smiseth OA.** Grading of myocardial dysfunction by tissue Doppler echocardiography: a comparison between velocity, displacement, and strain imaging in acute ischemia. *J Am Coll Cardiol* 47: 1672–1682, 2006.

30. **Tanaka N, Tone T, Ono S, Tomochika Y, Murata K, Kawagishi T, Yamazaki N, Matsuzaki M.** Predominant inner-half wall thickening of left ventricle is attenuated in dilated cardiomyopathy: an application of tissue Doppler tracking technique. *J Am Soc Echocardiogr* 14: 97–103, 2001.

31. **Torry RJ, Myers JH, Adler AL, Liut CL, Gallagher KP.** Effects of nontransmural ischemia on inner and outer wall thickening in the canine left ventricle. *Am Heart J* 122: 1292–1299, 1991.

32. **Uematsu M, Miyatake K, Tanaka N, Matsuda H, Sano A, Yamazaki N, Hirama M, Yamagishi M.** Myocardial velocity gradient as a new indicator of regional left ventricular contraction: detection by a two-dimensional tissue Doppler imaging technique. *J Am Coll Cardiol* 26: 217–223, 1995.

33. **Urheim S, Edvardsen T, Torp H, Angelsen B, Smiseth OA.** Myocardial strain by Doppler echocardiography. Validation of a new method to quantify regional myocardial function. *Circulation* 102: 1158–1164, 2000.

34. **Weidemann F, Dommke C, Bijnens B, Claus P, D'hooge J, Mertens P, Verbeken E, Maes A, Van de Werf F, De Scheerder I, Sutherland GR.** Defining the transmurality of a chronic myocardial infarction by ultrasonic strain-rate imaging: implications for identifying intramural viability: an experimental study. *Circulation* 107: 883–888, 2003.

35. **Weiss HR, Neubauer JA, Lipp JA, Sinha AK.** Quantitative determination of regional oxygen consumption in the dog heart. *Circ Res* 42: 394–401, 1978.

36. **Williams RI, Payne N, Phillips T, D'hooge J, Fraser AG.** Strain rate imaging after dynamic stress provides objective evidence of persistent regional myocardial dysfunction in ischaemic myocardium: regional stunning identified? *Heart* 91: 152–160, 2005.

Reversible vagal blockade in conscious rats using a targeted delivery device

Can Zheng [a,*], Toru Kawada [a], Meihua Li [a], Takayuki Sato [b],
Kenji Sunagawa [c], Masaru Sugimachi [a]

[a] Department of Cardiovascular Dynamics, Advanced Medical Engineering Center, National Cardiovascular Center Research Institute,
5-7-1 Fujishirodai, Suita-shi, Osaka 565-8565, Japan
[b] Department of Physiology, Kochi Medical School, Kochi 783-8505, Japan
[c] Department of Cardiovascular Medicine, Graduate School of Medical Sciences, Kyushu University, Fukuoka 812-8582, Japan

Abstract

Reversible methods of nerve blockade greatly aid neurophysiological and behavioral studies. We have developed an implantable device for the local delivery of anesthetics to the area surrounding the vagal nerve in rats. The device consists of a thick silicone tube for insulating the nerves from the surrounding tissue, and a thin silicone tube for the infusion of anesthetics into the insulating tube. The in vivo performance of the device was tested electrophysiologically, and cardiovascular responses to vagal stimulation were measured in conscious animals. Nerve conductivity was completely blocked by injection of a small amount ($<20\,\mu l$) of 1% lidocaine, with conductivity subsequently recovering gradually after 10–40 min. Electrical stimulation of the right vagus nerve in conscious rats increased arterial pressure while decreasing heart rate. The local blockade of afferent fibers abolished the arterial pressure response but preserved the bradycardic response to vagal nerve stimulation. The targeted delivery device was useful for reversible vagal blockade in conscious rats.
© 2006 Elsevier B.V. All rights reserved.

Keywords: Vagus; Conduction blockade; Electric stimulation; Heart rate; Blood pressure; Conscious; Rat

1. Introduction

Peripheral nerves are the first step in the pathway that conducts signals from various peripheral sensors to the central nervous system (CNS) and are also the output pathway for signals from the CNS to various organs, with most peripheral nerves containing both afferent and efferent fibers. In the investigation of the integrative functions of the autonomic nervous system, several techniques have been developed for performing nerve blockade for recording or selectively stimulating either afferent or efferent fibers. One such technique is surgical denervation, which effectively eliminates nerve conduction, but is irreversible and may not be applicable to the vagus nerve in the chronic experimental settings, as animals cannot survive for long after bilateral vagotomy. Nerve cooling provides a reversible nerve blockade in conscious large animals (Derksen et al., 1981;

Borgdorff and Versteeg, 1984; Cudd, 1998) and in anesthetized small animals (Vizek et al., 1983; Schultz et al., 1988; Lee et al., 1990), but is difficult in conscious small animals such as rats, due to technical problems associated with the size of the nerve cooling device. Alternatively, local anesthetics such as lidocaine are widely used for nerve blockade in clinical practice and animal studies (Thalhammer et al., 1995; Gokin et al., 2001; Potocnik et al., 2001). The major advantages of anesthetics for nerve blockade are the complete reversibility of the nerve blockade and the ease of administration. However, it can be difficult to administer local anesthetics in small conscious animals, largely because the vagus nerve runs close to the common carotid artery and the aortic depressor nerve, and therefore the injection procedure may result in artery or nerve damage. A technique of delivering neurotrophins or anesthetics to the sciatic nerve has been demonstrated in the conscious rat model (Kanje et al., 1988; Costanzo et al., 1999). However, it is not yet known whether such a targeted delivery method can be used to block the vagus nerve in conscious rats. In this study, we designed a targeted delivery device for the rat vagus nerve, which allowed local

* Corresponding author. Tel.: +81 6 6833 5012x2427; fax: +81 6 6835 5403.
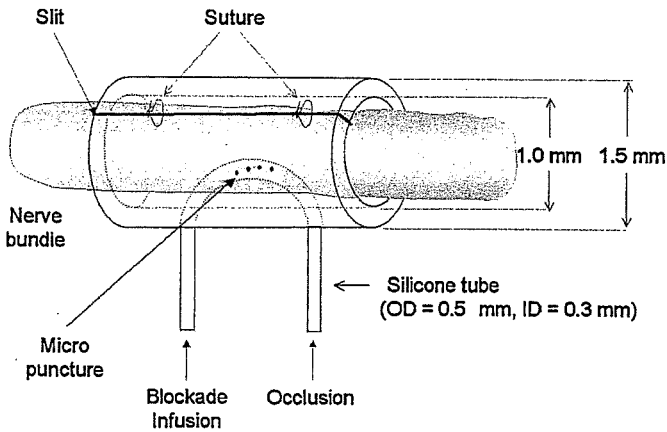E-mail address: zhengcan@ri.ncvc.go.jp (C. Zheng).

Fig. 1. Schematic illustration of the design of the targeted delivery device for the rat vagus nerve.

infusion of anesthetics into the area surrounding the nerve. The aim of this study was to evaluate this targeted delivery device for vagal blockade in conscious rats.

2. Materials and methods

2.1. A targeted delivery device

We designed an implantable device for delivering anesthetics to the area surrounding the rat cervical vagus nerve. As shown in Figs. 1 and 2E, this device was composed of a thick silicone tube (i.d. = 1.0 mm; o.d. = 1.5 mm; L = 3–4 mm) acting as a nerve guiding tube, and a thin silicone tube (i.d. = 0.3 mm; o.d. = 0.5 mm) for the injection of anesthetic agents. We made a longitudinal slit in the thick tube and pierced two holes in the wall of this tube for the thin tube to pass in and out of. Several micro-punctures were made by a microneedle (with a tip of 0.01 mm) in the inner part of the thin tube to allow the anesthetics to leak out into the guide tube.

We injected anesthetics slowly from one end of the thin tube until the liquid anesthetics replaced the air in the tube, and then we occluded the other end while increasing the pressure

in the thin tube to force the liquid to leak out through the micro-punctures into the area surrounding the nerve. In the present study, we used 1% lidocaine solution for local blockade of vagal conduction. After completion of the experimental protocol, we flushed the tubes with distilled water to prevent the micro-punctures from becoming occluded by residual anesthetics.

2.2. Surgical preparation

Experiments were performed on six Sprague–Dawley rats weighing between 320 and 450 g. Animals were cared for in strict accordance with the Guiding Principles for the Care and Use of Animals in the Field of Physiological Science approved by the Physiological Society of Japan. Under 1.5%-halothane anesthesia, the lead wires of the cuff electrodes and the infusion tubes were tunneled subcutaneously from the back where they were fixed to a custom-designed multi-channel skin connector (Fig. 2B and G). The right vagus nerve was carefully dissected away from the common carotid artery and placed into the guide tube. The slit in the guide tube was then sutured by a polypropylene suture (8-0, ETHICON, INC.). Two custom-designed cuff electrodes, each having a pair of stainless steel wire electrodes (Fig. 2F), were implanted into the nerve trunk in the proximal and distal sides of the guide tube at a distance of 1.1–1.4 mm. Next, a blood pressure telemeter (TA11PA-C40, DSI) was implanted into the abdomen with a pressure sensor inserted into the abdominal aorta for monitoring mean arterial pressure (MAP) and heart rate (HR). After recovery from the surgical procedure, the animals were maintained on standard rat chow ad libitum, and were restrained in a rodent cage for physiological measurements as described below.

2.3. Experimental protocols

The experimental protocols were conducted at least 1 week after the implantation surgery. The in vivo effectiveness of the targeted delivery for nerve blockade was evaluated electrophysiologically and by measurement of HR and MAP responses to
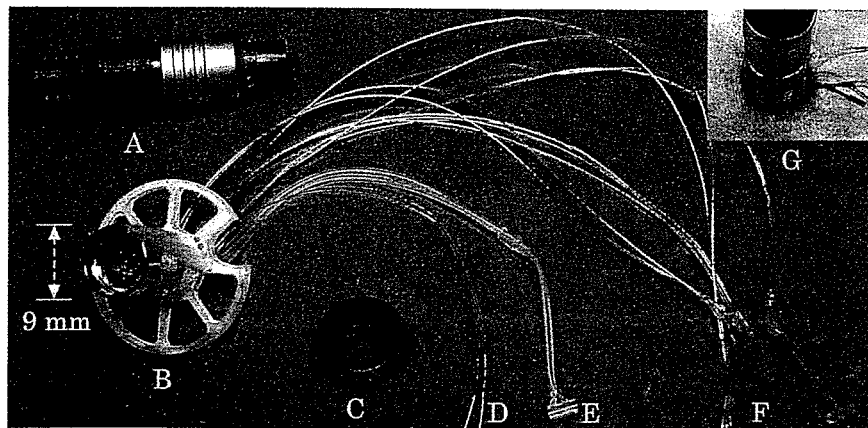

Fig. 2. Photographic images of the multi-channel skin connector with electrodes and nerve blocker. (A) Plug, (B) skin connector with 12-pin receptacle, (C) cap, (D) ECG leads, (E) nerve blocker, (F) nerve electrodes, the leads were extended with flexible coil (made of stainless wire of 0.03 mm in diameter, epoxy coated) and tips were fixed in the slit silicone tube (i.d. = 0.5; o.d. = 1 mm), and (G) implanted skin connector with local infusion setting.
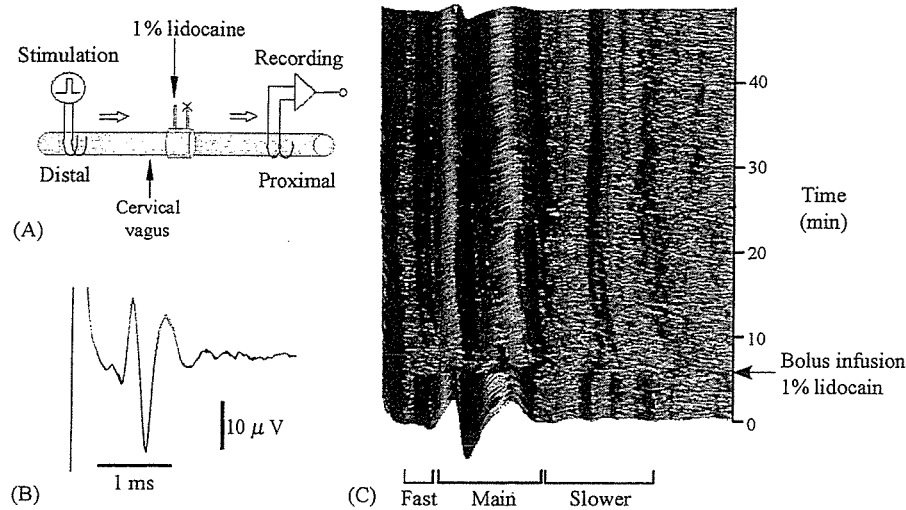
Fig. 3. Example of in vivo electrophysiology of the rat vagus. (A) A diagram of the experimental arrangement. (B) Compound action potential (CAP) of the right vagus evoked by the electrical pulse (1 Hz, 0.3 ms, 1.3 V). (C) The inhibition of vagal conduction by local injection of a small amount (<20 μl) of 1% lidocaine in conscious rats. Each trace was obtained as a result of waveform averaging of 10 single successive sweeps.

electrical stimulation of the vagus nerve in conscious animals. While the rat was loosely restrained in a rodent cage, lead wires for nerve stimulation and recording were attached to the skin connector (Fig. 2A and B). Arterial pressure was measured by telemetry. After carefully arranging the two electrodes and the delivery device, nerve stimulation with either distal or proximal nerve blockade was performed.

Nerve impulses were evoked by electrical stimulation of the vagus from the cuff electrode distal to the targeted delivery device (Fig. 3A). Rectangular pulses were delivered using a stimulator (SEN-7103, Nihon Kohden) and an isolator (SS-202J, Nihon Kohden). For in vivo electrophysiology, the stimulation frequency was 1 Hz and the pulse duration was 0.3 ms. The magnitude of stimulation was set at a supramaximal level (1.2–2.0 V). For functional experiments examining the AP and HR responses, the stimulation frequency, pulse duration, and magnitude were set at 10–30 Hz, 0.2–1 ms, and 2 V, respectively. The compound action potential (CAP) was amplified using an AC amplifier (200,000×, Model AB-610J, Nihon Kohden) with low (150 Hz) and high (1 kHz) frequency cutoffs. Nerve signals and arterial pressure data were sampled using a 12-bit A/D converter. Nerve signals were digitized at 5 kHz per electrode channel. The data were saved onto the hard disk of a dedicated laboratory computer system for later analysis.

2.4. Statistics

Data were reported as mean ± S.D. values. Changes in HR and MAP were compared before and during the stimulation by paired t-tests with the significance level set at $p < 0.05$.

3. Results

Fig. 3B shows the CAP of the vagus nerve evoked by electrical stimulation from the cuff electrode. The CAP consisted of one main component propagating at 0.9–2.1 m/s, as well as fast

(>3 m/s) and slow (<0.9 m/s) components. All components of the CAP disappeared after an injection of a small amount (<20 μl) of 1% lidocaine (Fig. 3C). The fast component had almost recovered 15 min after the injection, followed by recovery of the main component in 40 min. The slow component required longer to recover.

The rats stayed quiet during the injection of anesthetics, with no changes in baseline HR and MAP. The HR and AP responses to electric stimulation differed after blockade of the afferent nerves, compared with before blockade. Prior to nerve blockade, electric stimulation of the right vagus nerve decreased HR abruptly, whereas it was associated with an increase in MAP, as shown in Fig. 4; HR decreased from 434 ± 8 to 246 ± 35 bpm ($p < 0.01$), whereas MAP increased from 99 ± 11 to 127 ± 14 mmHg ($p < 0.01$). However, after the blockade of afferent fibers, electrical stimulation of the nerve decreased HR without significant changes in MAP (HR 414 ± 4 bpm versus 266 ± 17 bpm, $p < 0.01$; MAP 106 ± 12 mmHg versus 103 ± 14 mmHg). The effects of vagal afferent blockade were
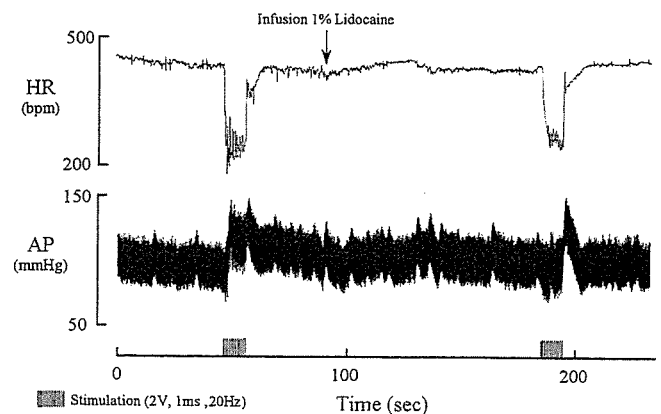

Fig. 4. Representative responses of arterial pressure (AP) and heart rate (HR) to electric stimulation (2 V, 1 ms, 20 Hz, 10 s) of the right vagus nerve before and after blockade of afferent fibers by local infusion of 1% lidocaine in conscious rats.
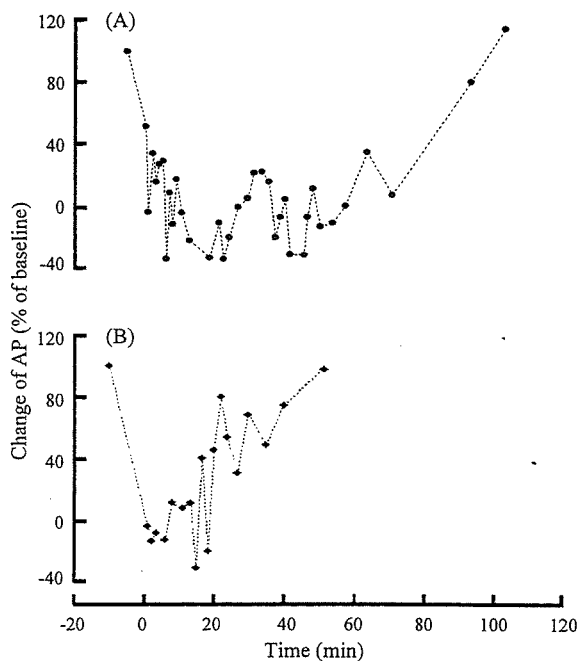
Fig. 5. Examples of the time course of the arterial pressure (AP) response to electric stimulation of cervical vagus nerve after afferent blockade by bolus infusion of 1% lidocaine in conscious rats. Each point represents the percentage of AP responses compared to the baseline response (before afferent blockade). Electric stimulations (2 V, 1 ms, 20 Hz, 10 s) were performed intermittently at interval greater than 1 min. The tests were done 1 week (A) and 2 weeks (B) after the implantation surgery.

reversible and the HR and MAP responses were restored in 15–60 min after the injection of 1% lidocaine. The duration of the nerve block was shorter in the second week than the first week (Fig. 5). The durability of the targeted delivery device was chiefly determined by how intact the infusion tube was. The effectiveness of the local blockade was confirmed 2 months after the implantation surgery.

4. Discussion

A variety of disease models, ranging from hypertension to heart failure, make the rat very important as an experimental animal for cardiovascular research. Reversible blockade of the autonomic nerves in small animals like the rat would be useful for physiological and behavioral study (Thalhammer et al., 1995), and would contribute to our understanding of the regulation of the cardiovascular system by the autonomic nervous system. We designed a targeted delivery device for the rat cervical vagus nerve. Using the targeted delivery device, in vivo electrophysiology and the functional evaluation of reversible nerve blockade were conducted in chronically instrumented, conscious rats. To our knowledge, this is the first study applying the targeted delivery device to blockade of the vagus nerve in conscious rats.

As shown in Fig. 3C, local injection of a small amount (<20 μl) of anesthetic (1% lidocaine) caused reversible, complete conduction block of the vagus nerve. The rats stayed calm in the rodent cage without any indication of significant stress

during or after the injection of anesthetics. Temporary administration of anesthetics via the targeted delivery device lessens the stress compared to other techniques of nerve blockade requiring surgical procedures, and is therefore suitable for evaluating the role of the autonomic nervous system in circulatory regulation without significant sympathetic excitation associated with the stress. The infusion period and the type of anesthetics may control the duration of nerve blockade. For instance, lidocaine causes a relatively short-lived nerve blockade whereas marcaine causes a longer blockade. Selective anesthetics may also be used for vagal afferent blockade (Bowser-Riley et al., 1990). Fig. 5 shows that the duration of the nerve block lessoned over time after the implantation surgery even with the same dose of anesthetic. The space surrounding the nerve within the guide tube may be replaced by regenerated tissue over time after the surgical procedure, possibly reducing the effective volume of distribution for the anesthetic. Although vagal blockade has been reported to increase HR in large animals like ponies (Derksen et al., 1981), the vagal blockade did not increase baseline HR significantly in rats in the present study. The differences in the effects of vagal blockade on HR may be a result of species difference in basal vagal nerve activity.

The autonomic nerves usually contain both afferent and efferent fibers. Hence the selective stimulation or recording of either the afferent or efferent nerve is essential to assess the role of the autonomic nerves in circulatory regulation. Vagal afferent fibers conduct the signals from most of the organs in the thoracic and abdominal cavity to the medulla, stimulating various viscerogenic reflexes. Continuous electrical stimulation of the afferent fibers may exert intensity-dependent inhibition of breathing, anxiety, or even painful behavioral reactions, often accompanying the increase in arterial pressure. As shown in Fig. 4, prior to nerve blockade, right vagal stimulation decreased HR and increased MAP, and the increase in MAP was not observed after blocking the portion proximal to the stimulation electrodes, suggesting that the increase in MAP before the proximal blockade could be attributed to vagal afferent activation. Combining vagal afferent blockade with vagal stimulation, we were able to selectively evaluate the role of the vagal efferent function in conscious rats (Li et al., 2003).

In conclusion, we have demonstrated a reversible blockade of the vagus nerve in conscious rats. A complete conduction block was achieved by local administration of a minimal dose of anesthetics. The reversible nerve blockade can be combined with nerve stimulation or nerve recording techniques to stimulate or record the efferent or afferent autonomic nerve activity in conscious animals. This technique, involving the use of a targeted delivery device, has the potential to aid in furthering our understanding of the role of the autonomic nervous system in cardiovascular regulation, and to promote physiological and behavioral studies.

Acknowledgements